LITHOS 468-469 (2024) 107513

Contents lists available at ScienceDirect

LITHOS

journal homepage: www.elsevier.com/locate/lithos

A revision of the Ni-in-garnet geothermometer with special regard to its pressure dependence

Paolo Nimis [a,*], Alberto Zanetti [b], Leander Franz [c]

[a] Department of Geosciences, University of Padua, Via G. Gradenigo 6, 35131 Padua, Italy
[b] CNR Istituto di Geoscienze e Georisorse, Sezione di Pavia, Via A. Ferrata 1, 27100 Pavia, Italy
[c] Departement Umweltwissenschaften, Universität Basel, Bernoullistrasse 30, 4056 Basel, Switzerland

ARTICLE INFO

Keywords:
Garnet
Olivine
Nickel
Partitioning
Geothermometer

ABSTRACT

We have explored the effect of temperature (*T*) and pressure (*P*) on Ni partitioning between garnet and olivine in well-equilibrated mantle xenoliths from on-craton, marginal-craton and off-craton settings and in high-*P*–*T* experiments at natural Ni abundance. Contrary to previous evaluations, the xenolith and experimental data indicate that the *P* effect is not negligible, consistent with the significant volume change of the garnet–olivine Mg-Ni exchange reaction. The recognition of a *P* effect satisfactorily resolves the discrepancies observed using previous calibrations of the Ni-in-Grt geothermometer and provides a solution to the long-standing controversy as to which Ni-in-Grt geothermometer is best applied to natural chromian pyrope compositions. A recalibrated, *P*-dependent Ni-in-garnet geothermometer reproduces the pyroxene *T* estimates for the xenoliths and the *T* conditions of the experiments with a standard error of estimate of 44 °C. The *P* dependence (ca. 40 °C/GPa) is comparable to that of the garnet–olivine Fe–Mg exchange geothermometer. A small tendency to overestimate at $T < 900$ °C relative to two-pyroxene thermometry is observed, which is unrelated to garnet compositional parameters. A set of simplified, geotherm-referenced calibrations permit traditional use of the Ni-in-garnet geothermometer as a single-mineral method, provided the local geotherm is known or can be estimated or inferred.

1. Introduction

The Ni-in-garnet geothermometer (Canil, 1994, 1999; Griffin et al., 1989; Ryan et al., 1996; Sudholz et al., 2021) is widely used to estimate temperatures for mantle-derived peridotitic garnets. The method is based on temperature-dependent partitioning of Ni between garnet (Grt) and olivine (Ol). Since the Ni content of mantle olivine usually varies over a restricted range (2900 ± 360 ppm, Ryan et al., 1996) and is much higher than that in garnet (10 to 200 ppm), mantle temperature (*T*) can be estimated directly from the Ni content of garnet alone. In combination with minimum pressure (*P*) estimates obtained by Cr-in-Grt geobarometry, the Ni-in-Grt geothermometer has long been used to determine the 'stratigraphy' and thermal state of lithospheric mantle sections based on compositional data for kimberlite-borne xenocrysts (e.g., Griffin et al., 2002; Ryan et al., 1996). The Ni-in-Grt geothermometer has also been used to estimate the formation *T* of peridotitic diamonds, in which garnet commonly occurs separated from its original mineral assemblage (e.g., Davies et al., 2004; De Hoog et al., 2019; Griffin et al., 1992, 1993; Viljoen et al., 2014).

Despite the considerable success of Ni-in-Grt thermometry in unraveling the structure and evolution of cratonic mantle lithospheres, there is poor consensus as to which of the available formulations of the Ni-in-Grt geothermometer is the most robust. Ryan et al. (1996) updated an earlier version by Griffin et al. (1989) and calibrated it against independent *T* estimates for 98 mantle xenoliths spanning a range of mantle bulk compositions and geotherms (640–1550 °C, 2.0–6.8 GPa). The independent *T* estimates were calculated by using a combination of the olivine–garnet Fe–Mg exchange geothermometer of O'Neill and Wood (1979) and the orthopyroxene–garnet geobarometers of MacGregor (1974) and Brey and Köhler (1990). Ni concentrations in garnets were obtained by proton microprobe analysis. Canil (1994) recalibrated the Ni-in-Grt geothermometer based on experiments at 1200–1500 °C and 5–8 GPa. These experiments used enhanced Ni concentrations in order to facilitate electron microprobe analysis. Canil (1999) proposed a new experimental calibration at natural Ni abundances based on partly reversed experiments at 1200–1500 °C and 3–7 GPa, obtaining results more similar to his earlier calibration than to that of Ryan et al. (1996). For this second recalibration, Canil (1999) also included data from

* Corresponding author.
E-mail addresses: paolo.nimis@unipd.it (P. Nimis), alberto.zanetti@igg.cnr.it (A. Zanetti), leander.franz@unibas.ch (L. Franz).

https://doi.org/10.1016/j.lithos.2024.107513
Received 4 October 2023; Received in revised form 12 January 2024; Accepted 16 January 2024
Available online 20 January 2024

melting experiments on natural peridotite by Canil (1994; two experiments at 1600–1700 °C and 5 GPa) and Herzberg and Zhang (1996; three experiments at 1726–2040 °C and 5–14 GPa). Ni concentrations in all these experiments were analyzed with an electron microprobe. Sudholz et al. (2021) recalibrated the Ni-in-Grt geothermometer against new experiments in a narrower *P*–*T* range (1100–1325 °C and 2.5–4.5 GPa), with Ni concentrations in garnet analyzed by high-precision laser-ablation inductively coupled plasma mass spectrometry (LA-ICP-MS).

Fig. 7 in Sudholz et al. (2021) shows that none of the above formulations of the Ni-in-Grt geothermometer satisfactorily reproduce *T* estimates for mantle xenoliths based on pyroxene geothermometry, which has been proposed as the reference standard for mantle peridotites (Nimis and Grütter, 2010). Discrepancies using the Ryan et al. (1996) formulation are particularly large and randomly distributed over the *T* range of the lithospheric mantle (mostly within ±150 °C and up to ca. ±250 °C). Discrepancies using the Canil (1999) formulation are less scattered, but show distinct systematic deviations, suggesting overestimation at $T < 1050$ °C (up to ca. +150 °C at 800 °C) and underestimation at higher *T* (up to ca. –150 °C at 1300 °C). Discrepancies using the Sudholz et al. (2021) formulation show less scatter than the Ryan et al. (1996) formulation but more scatter than the Canil (1999) formulation, and still show systematic overestimation at low *T*. Since pyroxene geothermometers are very robust at least between 900 and 1400 °C (Nimis and Grütter, 2010), these discrepancies may reflect poor performance of the Ni-in-Grt geothermometers.

A Ni-in-Grt geothermometer can be viewed as a simplified version of an olivine–garnet Ni–Mg-exchange geothermometer controlled by the reaction.

$$\frac{1}{3}\,\mathrm{Mg_3Al_2Si_3O_{12}}_{\text{garnet}} + \frac{1}{2}\,\mathrm{Ni_2SiO_4}_{\text{olivine}} = \frac{1}{3}\,\mathrm{Ni_3Al_2Si_3O_{12}}_{\text{garnet}} + \frac{1}{2}\,\mathrm{Mg_2SiO_4}_{\text{olivine}}, \quad (1)$$

in which the equilibrium constant

$$\frac{\left(a_{\mathrm{Ni_3Al_2Si_3O_{12}}}\right)_{\mathrm{Grt}}^{1/3}\cdot\left(a_{\mathrm{Mg_2SiO_4}}\right)_{\mathrm{Ol}}^{1/2}}{\left(a_{\mathrm{Ni_2SiO_4}}\right)_{\mathrm{Ol}}^{1/2}\cdot\left(a_{\mathrm{Mg_3Al_2Si_3O_{12}}}\right)_{\mathrm{Grt}}^{1/3}}$$

is assumed to be essentially controlled by $\left(a_{\mathrm{Ni_3Al_2Si_3O_{12}}}\right)_{\mathrm{Grt}}$ variations. There is general agreement that reaction (1) is sensitive to *T* and insensitive to *P* and, in fact, none of the available formulations of the Ni-in-Grt geothermometer includes a *P* term. Indeed, existing high-*P*, high-*T* experiments on the partitioning of Ni between garnet and olivine did not reveal any clear *P* effect within their respective *P*–*T* intervals (Canil, 1994, 1999; Sudholz et al., 2021; Yaxley and O'Neill, 2008). This is surprising, since the estimated ΔV°_{298} for reaction (1) is not negligible (0.13 J/bar; Canil, 1994) and other exchange reactions between garnet and olivine that are used as geothermometers and have a smaller ΔV°_{298} have a significant *P*-dependence (e.g., ca. 50 °C/GPa for the Fe–Mg exchange geothermometer with $\Delta V^{\circ}_{298} = 0.07$ J/bar; Wu and Zhao, 2007). Moreover, Yaxley and O'Neill (2008) noted that different calibrations of the Ni-in-Grt geothermometer reproduced best independent *T* estimates for mantle xenoliths when their equilibrium pressures were close to their respective calibration *P* ranges, suggesting a possible unresolved *P* effect of ca. 60–80 °C/GPa. Therefore, the *P* dependence of the garnet–olivine Ni partitioning deserves further analysis.

Here, we revisit the relationships between Ni-in-Grt, *T*, and *P* in a large dataset of well-equilibrated mantle xenoliths from both on-craton and off-craton settings. The advantage of using natural samples is that they cover a wide range of *P*–*T* conditions and compositions, which reduces the need for major extrapolations in subsequent applications. Nonetheless, a major disadvantage of empirical calibrations using natural samples is that they heavily rely on the accuracy of the *P*–*T* estimates on which they are based. Our study intentionally covers a broad *P* range over typical lithospheric temperatures (Fig. 1), in order to achieve better discrimination of *T* and *P* effects on Ni uptake in natural peridotitic garnet compositions than was possible with previous experimental calibrations (Canil, 1994, 1999; Sudholz et al., 2021). We also exercise tighter control on xenolith mineral equilibria and accuracy of thermobarometric results than was the case in the Ryan et al. (1996) empirical Ni-in-Grt calibration, thus minimizing uncertainties in the input data for this study.

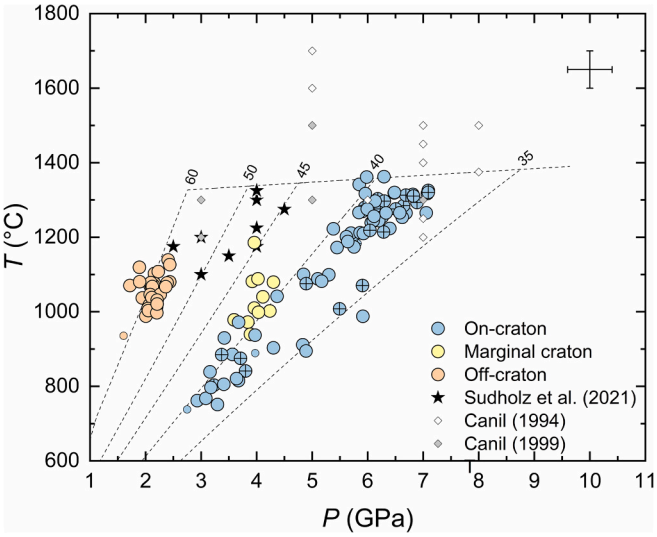

Fig. 1. *P*–*T* data for datasets used for previous and present calibrations of the Ni-in-Grt geothermometer. Circles indicate mantle xenoliths for which *P*–*T* were estimated through a combination of the Taylor (1998) two-pyroxene geothermometer and the Nickel and Green (1985) orthopyroxene–garnet geobarometer (as corrected by Carswell, 1991) or through single-clinopyroxene geothermobarometry (Nimis and Taylor, 2000; with corrections by Nimis et al., 2020). Crossed circles indicate samples for which only a partial equilibrium check could be performed (see text). Small circles indicate samples that were outliers in the $\ln D_{\mathrm{Ni}}$ vs. reciprocal *T* plot (cf. Fig. 3) and were not used for the geothermometer recalibration. Other symbols indicate experiments on olivine–garnet Ni partitioning used for previous calibrations of the same geothermometer. Representative error bars for the xenoliths (±50 °C; ±0.4 GPa) consider uncertainties in geothermobarometer calibrations, analytical uncertainties and the mutual dependence of *P* and *T* estimates (Nimis and Grütter, 2010). Model conductive geotherms up to the mantle adiabat for different surface heat flows are shown for comparison (in mW/m^2 after Hasterok and Chapman, 2011). The present recalibration uses data for both the xenoliths and the experiments of Sudholz et al. (2021) and thus covers *P*–*T* conditions for lithospheric mantle spanning a range of geotherms. (For interpretation of the references to colour in this figure legend, the reader is referred to the web version of this article.)

2. The dataset

Our xenolith dataset includes published and unpublished data for $\mathrm{Ni_{Grt}}$ (proton microprobe or laser-ablation inductively coupled plasma mass spectrometry analyses) in mantle lherzolites from representative on-craton ($N = 80$) and off-craton ($N = 22$) mantle sources (Table 1). In order to improve the leverage of *P*–*T* data, additional 6 mantle peridotite xenoliths from the off-craton Pali Aike volcanic field (Patagonia, Argentina–Chile; Rivalenti et al., 2004) and 11 xenoliths from the marginal-craton Gibeon province (Namibia; Franz et al., 1996) were selected for this study and analyzed by LA-ICP-MS at IGG-CNR, Pavia (Italy). The laser probe consists of a QQQ-ICP-MS Agilent Series 8900 coupled with a UP213 deep-UV YAG Laser Ablation System (New Wave Research, Inc.). The laser was operated at a repetition rate of 10 Hz, with 213 nm wavelength and a fluence of ~9.5 J/cm^2. Helium was used as carrier gas and was mixed with Ar downstream of the ablation cell. Spot diameter was 55 μm. Data reduction was performed offline using the GLITTER software. For this study, the NIST SRM 610 synthetic glass was

Table 1
Garnet and olivine compositions and thermobarometry of samples used for Ni-in-Grt geothermometer recalibration.

Label	Source	Locality	Grt *X*Ca	Grt *X*Cr	Grt Ni (ppm)	Ol Ni (ppm)*	Ol NiO (wt%)#	*P* (GPa) NG85	*T* (°C) TA98	*T* (°C) RY96	*T* (°C) CN99	*T* (°C) SU21	*T* (°C) Eq. (2)	*T* (°C) Ca-in-Opx	*P* (GPa) NT00
ON CRATON															
MX032	Creighton et al. (2010)	Diavik	0.176	0.298	64.71	–	0.32	6.06	1239	1120	1112	1309	1187	1212	6.31
MX044	Creighton et al. (2010)	Diavik	0.127	0.127	83.90	–	0.29	6.48	1320	1222	1171	1227	1270	1306	7.00
MX088	Creighton et al. (2010)	Diavik	0.138	0.170	41.45	–	0.26	5.75	1174	974	1021	1085	1077	1133	5.95
MX104	Creighton et al. (2010)	Diavik	0.155	0.221	74.42	–	0.31	6.26	1255	1173	1143	1278	1230	1237	6.97
MX144	Creighton et al. (2010)	Diavik	0.107	0.052	70.06	–	0.32	6.62	1253	1150	1130	1122	1229	1241	6.71
MX165	Creighton et al. (2010)	Diavik	0.170	0.261	72.86	–	0.33	6.20	1245	1165	1139	1314	1222	1225	6.48
MX5001	Creighton et al. (2010)	Diavik	0.136	0.162	62.43	–	0.33	6.10	1244	1107	1104	1177	1180	1222	6.76
MX5003	Creighton et al. (2010)	Diavik	0.161	0.173	15.15	–	0.33	4.30	903	735	854	906	850	834	4.52
MX5004	Creighton et al. (2010)	Diavik	0.151	0.204	61.73	–	0.33	5.70	1211	1103	1102	1212	1162	1190	6.27
MX5006	Creighton et al. (2010)	Diavik	0.156	0.236	63.72	–	0.32	5.86	1212	1114	1109	1245	1176	1194	6.28
MX5008	Creighton et al. (2010)	Diavik	0.133	0.135	55.62	–	0.26	6.33	1265	1067	1080	1131	1162	1255	6.57
MX5009	Creighton et al. (2010)	Diavik	0.149	0.216	76.11	–	0.31	5.99	1275	1182	1149	1276	1224	1254	6.12
MX5012	Creighton et al. (2010)	Diavik	0.128	0.161	49.54	–	0.36	5.62	1201	1028	1056	1115	1109	1176	5.75
A154-09CR	Creighton et al. (2010)	Diavik	0.118	0.110	45.11	–	0.37	5.30	1099	999	1037	1060	1077	1066	5.10
RVD100	Viljoen et al. (2009)	Premier	0.108	0.052	111	–	0.36	6.29	1363	1351	1241	1241	1339	1355	5.75
RVD101	Viljoen et al. (2009)	Premier	0.135	0.174	151	–	0.38	5.91	1325			*Outlier*		1328	5.69
RVD106	Viljoen et al. (2009)	Premier	0.128	0.158	138	–	0.40	5.85	1342	1467	1300	1401	1384	1334	5.55
RVD155	Viljoen et al. (2009)	Premier	0.113	0.059	44.1	–	0.47	3.42	930	992	1033	1028	1002	933	3.29
RVD181	Viljoen et al. (2009)	Premier	0.135	0.180	63.1	–	0.40	4.84	1100	1111	1107	1190	1133	1113	4.20
RVD190	Viljoen et al. (2009)	Premier	0.114	0.097	119	–	0.38	5.98	1361	1386	1260	1295	1345	1347	5.79
RVD197	Viljoen et al. (2009)	Premier	0.095	0.062	38.6	–	0.39	3.67	972	953	1008	992	986	960	3.12
F05JM1	Gibson et al. (2008)	Finsch	0.138	0.193	58.13	–	–	5.45	1172	1082	1089	1179	1138	1163	5.49
F05JM2	Gibson et al. (2008)	Finsch	0.121	0.108	74.63	–	0.38	5.64	1188	1174	1144	1180	1205	1173	5.90
F05JM7	Gibson et al. (2008)	Finsch	0.127	0.154	71.71	–	0.39	5.92	1210	1159	1135	1202	1207	1182	5.85
BD3692	Gibson et al. (2008)	Finsch	0.108	0.092	51.22	–	0.44	5.10	1088	1039	1063	1072	1097	1065	4.57
BD3693	Gibson et al. (2008)	Finsch	0.106	0.093	31.53	–	0.42	5.17	1082	898	971	973	1002	1068	4.68
KBD12	Hanger et al. (2015)	Wesselton	0.102	0.166	49.7	–	0.38	4.37	1042	1029	1057	1100	1062	1107	4.14
JJH28	Mofokeng (1998)	Jagersfontein	0.126	0.089	77	–	0.38	5.38	1222	1187	1151	1180	1202	1196	5.23
JJH7	Mofokeng (1998)	Jagersfontein	0.134	0.153	101	–	0.35	5.96	1317	1305	1217	1304	1298	1302	5.98
JAG90–10	Grégoire et al. (2003)	Jagersfontein	0.150	0.190	39	1742	0.22	3.97	937	956	1010	1091	999	963	4.83
JAG90–12	Grégoire et al. (2003)	Jagersfontein	0.122	0.140	33	2044	0.26	2.75	738			*Outlier*		794	3.25
BD2379	Grégoire et al. (2003)	Bultfontein	0.138	0.116	23	2636	0.34	3.56	885	822	918	943	891	837	3.79
rom194	Grégoire et al. (2003)	Monastery	0.120	0.014	31	1882	0.24	3.16	839	894	968	944	927	871	3.66
LBM36–2	Mofokeng (1998)	Matsoku	0.115	0.053	48	–	0.47	4.89	1076	1018	1050	1044	1075	1044	–
U10	Ionov et al. (2010)	Udachnaya	0.172	0.291	120	3858	0.49	6.16	1293	1390	1262	1511	1356	1288	6.86
U29	Ionov et al. (2010)	Udachnaya	0.166	0.187	25.0	–	–	4.83	911	841	931	1006	948	949	4.01
U50	Ionov et al. (2010)	Udachnaya	0.136	0.143	91.1	–	–	5.95	1280	1258	1191	1267	1269	1283	6.93
U57	Ionov et al. (2010)	Udachnaya	0.177	0.358	199.4	3078	0.39	5.90	1269			*Outlier*		1259	6.44
U64	Ionov et al. (2010)	Udachnaya	0.163	0.337	51.7	3110	0.40	5.73	1198	1042	1065	1258	1123	1155	6.19
U71	Ionov et al. (2010)	Udachnaya	0.145	0.177	84.8	3734	0.48	5.84	1266	1227	1174	1278	1246	1283	6.74
U85	Ionov et al. (2010)	Udachnaya	0.102	0.059	74.0	–	–	6.69	1265	1171	1142	1135	1246	1257	6.84
U148	Ionov et al. (2010)	Udachnaya	0.129	0.141	115	–	–	6.23	1276	1368	1250	1329	1346	1270	–
U183	Ionov et al. (2010)	Udachnaya	0.168	0.273	79.8	3650	0.46	6.40	1224	1201	1160	1348	1253	1218	6.99
U260	Ionov et al. (2010)	Udachnaya	0.184	0.213	138	–	–	3.97	889			*Outlier*		881	3.98
U267	Ionov et al. (2010)	Udachnaya	0.108	0.077	109.5	–	–	6.65	1285	1344	1238	1253	1350	1300	–
U283	Ionov et al. (2010)	Udachnaya	0.160	0.146	19.6	–	–	2.93	762	787	892	938	844	827	3.15
U501	Ionov et al. (2010)	Udachnaya	0.139	0.158	28.5	–	–	4.89	895	873	953	1002	974	913	3.90
U506	Ionov et al. (2010)	Udachnaya	0.163	0.190	35.2	–	–	5.91	988	928	991	1077	1050	1031	4.93
U507	Ionov et al. (2010)	Udachnaya	0.108	0.078	105	–	–	6.81	1315	1322	1226	1241	1345	1314	–
U532	Ionov et al. (2010)	Udachnaya	0.161	0.311	144	–	–	6.03	1291			*Outlier*		1268	6.48
Uv-268/02	Agashev et al. (2013)	Udachnaya	0.107	0.081	104.1	–	0.38	7.07	1317	1319	1225	1241	1354	1302	–
Uv-38/02	Agashev et al. (2013)	Udachnaya	0.136	0.173	85.5	–	0.38	6.50	1276	1230	1176	1270	1276	1245	–

(*continued on next page*)

Table 1 (*continued*)

Label	Source	Locality	Grt *X*Ca	Grt *X*Cr	Grt Ni (ppm)	Ol Ni (ppm)*	Ol NiO (wt%)#	*P* (GPa) NG85	*T* (°C) TA98	*T* (°C) RY96	*T* (°C) CN99	*T* (°C) SU21	*T* (°C) Eq. (2)	*T* (°C) Ca-in-Opx	*P* (GPa) NT00
Uv-97/02	Agashev et al. (2013)	Udachnaya	0.110	0.127	91.4	–	0.33	6.89	1293	1259	1192	1236	1310	1268	–
Uv-1/04	Agashev et al. (2013)	Udachnaya	0.126	0.149	81.3	–	0.32	6.29	1214	1209	1164	1231	1253	1227	–
Uv-213/02	Agashev et al. (2013)	Udachnaya	0.159	0.278	107.5	–	0.36	6.18	1303	1335	1233	1443	1325	1275	–
Uv-252/02	Agashev et al. (2013)	Udachnaya	0.126	0.149	131.2	–	0.36	6.69	1313	1439	1286	1375	1407	1302	–
Uv-205/02	Agashev et al. (2013)	Udachnaya	0.146	0.213	101.1	–	0.38	6.30	1297	1305	1217	1358	1312	1281	–
Uv-33/04	Agashev et al. (2013)	Udachnaya	0.146	0.215	89.8	–	0.32	6.82	1311	1251	1188	1322	1302	1294	–
Uv-257/02	Agashev et al. (2013)	Udachnaya	0.105	0.087	97.8	–	0.35	7.09	1326	1290	1209	1226	1337	1292	–
Uv-27/01 (Grt core)	Agashev et al. (2013)	Udachnaya	0.125	0.129	71.8	–	0.23	7.09	1320	1159	1135	1185	1254	1325	–
Uv-24/05	Agashev et al. (2013)	Udachnaya	0.143	0.228	107.6	–	0.34	6.48	1319	1336	1233	1387	1338	1308	–
Uv-153/02	Agashev et al. (2013)	Udachnaya	0.137	0.238	93.6	–	0.32	6.82	1310	1270	1198	1343	1313	1304	–
Uv-9-05	Yaxley et al. (2012)	Udachnaya	0.162	0.163	16.1	–	0.43	3.09	768	747	863	913	820	837	3.27
Uv-50-04	Yaxley et al. (2012)	Udachnaya	0.126	0.143	102	–	0.41	6.13	1297	1310	1220	1293	1308	1289	6.94
Uv129–03	Yaxley et al. (2012)	Udachnaya	0.126	0.121	97.8	–	0.38	5.82	1183			*Outlier*		1252	–
DalV91	Ashchepkov et al. (2017)	Dalnyaya	0.130	0.131	76.4	–	–	6.04	1219	1184	1149	1207	1227	1249	–
Dal35	Ashchepkov et al. (2017)	Dalnyaya	0.122	0.115	60.0	–	–	7.05	1265	1093	1096	1130	1209	1282	7.21
Dal34	Ashchepkov et al. (2017)	Dalnyaya	0.131	0.105	79.5	–	–	6.11	1256	1200	1159	1202	1240	1273	6.72
DalV10	Ashchepkov et al. (2017)	Dalnyaya	0.121	0.117	73.8	–	–	6.58	1266	1170	1141	1182	1241	1273	6.66
Z4–2	Ziberna et al. (2013)	Zagadochnaya	0.113	0.080	26.3	–	–	–	797[$]	853	940	939	902	–	3.09
Z5–02	Ziberna et al. (2013)	Zagadochnaya	0.128	0.146	23.0	–	–	–	865[$]	822	918	950	896	–	3.64
Z5–11	Ziberna et al. (2013)	Zagadochnaya	0.121	0.115	24.7	–	–	–	821[$]	838	929	946	911	–	3.70
Z5–15	Ziberna et al. (2013)	Zagadochnaya	0.110	0.036	22.0	–	–	–	878[$]	812	910	889	877	–	3.25
G1–3	Karen Smit (pers. comm.)	Grib	0.119	0.059	17.9	–	0.39	3.67	815	768	878	869	854	745	3.51
G1–5	Karen Smit (pers. comm.)	Grib	0.111	0.075	38.7	–	0.33	5.90	1071	954	1008	1008	1051	1045	–
G1–7	Karen Smit (pers. comm.)	Grib	0.114	0.083	39.8	–	0.38	5.49	1008	962	1013	1019	1040	1026	–
G1–13	Karen Smit (pers. comm.)	Grib	0.110	0.095	25.2	–	0.34	3.64	821	843	933	936	910	814	3.93
G1–14	Karen Smit (pers. comm.)	Grib	0.112	0.102	24.0	–	0.39	3.41	805	832	925	931	890	811	3.70
G1–23	Karen Smit (pers. comm.)	Grib	0.136	0.136	14.9	–	0.41	3.18	797	731	851	876	811	729	3.52
G1–25	Karen Smit (pers. comm.)	Grib	0.140	0.126	15.6	–	0.40	3.29	751	740	858	882	821	796	3.55
MARGINAL CRATON															
KGG45	This work + Franz et al. (1996)	Gibeon	0.121	0.079	39.8(11.6)	–	0.42	3.96	1010	962	1013	1021	1002	1027	3.86
KGG20B	This work + Franz et al. (1996)	Gibeon	0.127	0.080	34.7(7.4)	–	0.39	4.11	1040	924	988	998	982	1017	3.94
KGG14	This work + Franz et al. (1996)	Gibeon	0.123	0.076	44.2(2.8)	–	0.49	4.24	1002	993	1033	1042	1033	971	3.83
KGG50	This work + Franz et al. (1996)	Gibeon	0.126	0.086	33.9(3.3)	–	0.38	4.03	999	917	984	995	974	980	3.90
KGG60	This work + Franz et al. (1996)	Gibeon	0.121	0.070	38.3(4.1)	–	0.26	3.59	979	951	1006	1010	981	1009	3.60
KGG65	This work + Franz et al. (1996)	Gibeon	0.137	0.130	35.3(1.5)	–	0.38	3.84	972	929	991	1031	975	957	3.64
KGG88A	This work + Franz et al. (1996)	Gibeon	0.134	0.121	37.5(3.9)	–	0.37	3.89	940	945	1002	1038	988	957	3.63
KGG16	This work + Franz et al. (1996)	Gibeon	0.133	0.096	58.8(8.6)	–	0.40	3.92	1082	1086	1091	1123	1081	1098	4.01
KGG62A	This work + Franz et al. (1996)	Gibeon	0.132	0.120	52.0(6.0)	–	0.26	4.02	1088	1044	1066	1107	1059	1099	3.96
KGG55	This work + Franz et al. (1996)	Gibeon	0.121	0.072	47.9(4.9)	–	0.36	4.30	1080	1018	1049	1056	1052	1065	3.88
KGG44A	This work + Franz et al. (1996)	Gibeon	0.123	0.075	80.1(8.7)	–	0.39	3.96	1185	1203	1160	1180	1153	1236	4.06

(*continued on next page*)

Table 1 (*continued*)

Label	Source	Locality	Grt *X*Ca	Grt *X*Cr	Grt Ni (ppm)	Ol Ni (ppm)*	Ol NiO (wt%)#	*P* (GPa) NG85	*T* (°C) TA98	*T* (°C) RY96	*T* (°C) CN99	*T* (°C) SU21	*T* (°C) Eq. (2)	*T* (°C) Ca-in-Opx	*P* (GPa) NT00
OFF CRATON															
SW0169	Zheng et al., 2006	E China	0.135	0.057	74.7	2263	0.29	1.94	1037	1175	1144	1161	1054	1042	1.89
SW0193	Zheng et al., 2006	E China	0.124	0.029	78.2	2567	0.33	1.60	936	*Outlier*				933	1.36
SW01–1	Zheng et al., 2006	E China	0.126	0.022	74.3	2523	0.32	2.16	1103	1173	1143	1133	1062	1125	1.61
SW01–8	Zheng et al., 2006	E China	0.121	0.018	77.6	2561	0.33	2.23	1108	1190	1153	1137	1075	1092	1.36
SW04–2	Zheng et al., 2006	E China	0.120	0.016	71.5	2564	0.33	1.72	1071	1158	1134	1116	1036	1075	2.09
SW04–6	Zheng et al., 2006	E China	0.120	0.014	82.4	2517	0.32	1.89	1119	1215	1167	1150	1074	1107	1.55
8508–6	Nimis et al. (2015) + Ionov (pers. comm.)	Dariganga	0.133	0.045	80.9	–	0.42	2.08	1071	1207	1163	1173	1078	1077	2.11
8508–9	Nimis et al. (2015) + Ionov (pers. comm.)	Dariganga	0.135	0.037	73.8	–	0.38	2.16	1076	1170	1141	1147	1060	1104	2.14
BY-18	Nimis et al. (2015) + Ionov (pers. comm.)	Dariganga	0.130	0.047	70.9	–	0.41	2.10	1071	1155	1132	1139	1049	1116	2.05
BY-19	Nimis et al. (2015) + Ionov (pers. comm.)	Dariganga	0.130	0.041	69.7	–	0.39	2.14	1071	1148	1129	1132	1047	1107	2.05
BY-27	Nimis et al. (2015) + Ionov (pers. comm.)	Dariganga	0.130	0.039	71.5	–	0.31	2.09	1078	1158	1134	1137	1051	1112	1.98
BY-33	Nimis et al. (2015) + Ionov (pers. comm.)	Dariganga	0.134	0.044	69.0	–	0.31	2.12	1068	1144	1126	1133	1044	1093	2.14
198	Kopylova et al. (1995)	Shavaryn-Tsaram	0.118	0.021	65	–	–	1.89	1081	1122	1113	1096	1022	1085	1.62
SF-93163	Glaser et al. (1999)	Vitim	0.117	0.043	105	2840	0.36	2.40	1139	1323	1227	1228	1155	1083	2.12
SG-96B13	Glaser et al. (1999)	Vitim	0.124	0.026	47	2640	0.34	2.07	1019	1012	1045	1032	964	1030	1.96
313–6	Ionov (2004)	Vitim	0.121	0.039	65	–	–	2.08	1046	1122	1113	1108	1030	1054	2.07
313–102	Ionov (2004)	Vitim	0.122	0.027	65	–	0.39	2.26	1047	1122	1113	1101	1037	1044	2.02
313–104	Ionov (2004)	Vitim	0.122	0.030	66	–	–	2.11	1038	1127	1116	1107	1034	1057	2.01
313–106	Ionov (2004)	Vitim	0.121	0.029	63	–	0.41	2.00	988	1110	1106	1095	1020	1012	1.82
313–112	Ionov (2004)	Vitim	0.124	0.034	57	–	–	2.20	1014	1075	1085	1077	1007	1027	1.96
313–240	Ionov (2004)	Vitim	0.123	0.033	66	–	0.44	2.04	1008	1127	1116	1109	1031	1022	1.96
313–241	Ionov (2004)	Vitim	0.123	0.033	72	–	–	2.05	1003	1160	1136	1130	1051	1045	1.93
LA10A	This work	Pali Aike	0.128	0.049	68.3(2.3)	3092(7)	0.39	2.43	1080	1140	1143	1133	1055	1034	2.50
LA2	This work	Pali Aike	0.123	0.044	64.2(4.5)	3124(24)	0.40	2.21	1031	1117	1153	1137	1032	1036	2.28
LA4	This work	Pali Aike	0.126	0.055	67.8(1.6)	3126(99)	0.40	2.39	1077	1137	1134	1116	1051	1039	2.42
TA28	This work	Pali Aike	0.119	0.036	64.1(1.2)	3059(97)	0.39	2.21	1021	1117	1167	1150	1032	993	2.04
LA1	This work	Pali Aike	0.147	0.097	81.6(3.8)	3227(33)	0.41	2.43	1126	1211	1163	1173	1095	1113	2.53
LA11	This work	Pali Aike	0.131	0.050	60.8(1.8)	3208(55)	0.41	2.36	1067	1098	1141	1147	1027	1043	2.42
EXPERIMENTS								*P* (GPa)	*T* (°C)						
NIMPY5	Sudholz et al. (2021)		0.122	0.046	67.3	2800–3200§		3.0	1100	1135	1113	1112	1067		
NIMPY4	Sudholz et al. (2021)		0.111	0.045	92.0	2800–3200§		3.5	1150	1262	1185	1180	1160		
NIMPY9	Sudholz et al. (2021)		0.129	0.050	95.2	2800–3200§		4.0	1175	1278	1194	1205	1189		
NIMPY27	Sudholz et al. (2021)		0.102	0.046	89.5	2800–3200§		2.5	1175	1250	1179	1166	1111		
NIMPY10	Sudholz et al. (2021)		0.121	0.043	102.3	2800–3200§		3.0	1200	1311	1211	1214	1165		
NIMPY7	Sudholz et al. (2021)		0.102	0.045	126.3	2800–3200§		4.0	1225	1418	1266	1258	1265		
NIMPY28	Sudholz et al. (2021)		0.068	0.051	125.0	2800–3200§		4.5	1275	1412	1264	1229	1284		
NIMPY12	Sudholz et al. (2021)		0.064	0.045	173.2	2800–3200§		4.0	1300	1608	1357	1317	1359		
NIMPY13	Sudholz et al. (2021)		0.058	0.051	177.9	2800–3200§		4.0	1325	1625	1365	1324	1368		

TA98 – Taylor (1998) at P_{NG85}; NG85 – Nickel and Green (1985), with corrections by Carswell (1991), at T_{TA98}; RY96 – Ryan et al. (1996); CN99 – Canil (1999); SU21 – Sudholz et al. (2021); Ca-in-Opx – Brey and Köhler (1990) with corrections by Nimis and Grütter (2010); NT00 – Nimis and Taylor (2000), with corrections by Nimis et al. (2020).

* Ni data by LA-ICP-MS or proton-probe analysis (numbers in parentheses indicate standard deviations on three to ten analytical spots for the samples analyzed in this work);

\# NiO data by EMPA or, when available, recalculated from LA-ICP-MS data;

§ Values for individual experiments were not specified, only the overall range was given;

$ *T* calculated using the single-clinopyroxene geothermometer of Nimis and Taylor (2000).

used as external standard, CaO was used as internal standard for garnet and clinopyroxene, and SiO_2 was used as internal standard for coexisting olivine and orthopyroxene. Relative precision and accuracy of the Ni concentration values were assessed to be better than ±5% by repeated analysis of the BCR2-g and NIST SRM 612 standards. Three to ten spots were analyzed on one or more mineral grains and the results were averaged. Relative standard deviations on garnets were mostly within ~10%, indicating good homogeneity (Table 1). Two Gibeon samples showed much larger standard deviations (~20–30%), indicating less homogeneous compositions. These two samples were initially accepted with reserve, but were finally maintained, because they produced very low residuals in the subsequent regression analyses and their exclusion did not significantly change the regression results.

The analyzed Gibeon samples are a subset of the samples studied by Franz et al. (1996), who reported major element compositions of minerals. Major element compositions of minerals in the Pali Aike xenoliths (Table 2) were analyzed using a Tescan Solaris FE-SEM at Department of Geosciences, Padua (Italy), equipped with Oxford Instruments Ultim Max 65 EDS and Wave 700 WDS spectrometers. Analytical conditions were 15 kV and 15 nA. Si, Ca, Mg, Fe, Ni, Mn and Ti were measured by standardized EDS analysis, using a count time of 20 to 30 s. Al, Na, Cr and K were analyzed by standardized WDS analysis during the same analytical routine, using count times for peak of 10 to 15 s for K, 10 to 25 s for Al and Na, and 50 to 70 s for Cr, and count times for backgrounds of 5 s for K, Al and Na, and 20 to 25 s for Cr. These EDS–WDS conditions ensured nominal standard deviations of individual point analyses of ca. 0.03 wt% (absolute) or better for all analyzed elements. Standards for both EDS and WDS pyroxene analyses were natural diopside (for Si, Ca and Mg), albite (for Na), K-feldspar (for K), and pure synthetic Fe_2O_3, Al_2O_3, NiO, and $MnTiO_3$ (for Fe, Al, Ni, Mn and Ti). For garnet analyses, Mg and Al were calibrated on a natural pyrope. For spinel analyses, Mg was calibrated on synthetic MgO. For olivine analyses, Si and Mg were calibrated on a San Carlos olivine. EDS analyses of Ni, Mn and Ti in silicates were only made to ensure proper matrix corrections during EDS-WDS analysis, but the final accepted concentrations of these elements were those obtained by more precise LA-ICP-MS on the same mineral grains. Three to five EDS-WDS points were analyzed close to the LA-ICP-MS craters in core portions of the different minerals and the compositions were averaged (Table 1). Additional point analyses were taken close to the rims of pyroxene grains to check for chemical homogeneity. Overall, the grains were very homogeneous, except for minor changes in Al and Cr contents in some pyroxene rims. Only in sample LA2 a significant decrease in Al and Na and increase in Mg and Ca was observed near the clinopyroxene rim (Table 2).

Since accuracy of thermobarometric data is essential for the purpose of this work, several measures were taken to avoid spurious data and maintain uncertainties as low as possible. Following recommendations by Nimis and Grütter (2010), the *P–T* conditions for the new and literature samples were estimated or recalculated using a combination of the Taylor (1998) two-pyroxene geothermometer and the Nickel and Green (1985) orthopyroxene–garnet geobarometer. This combination reproduces best experimental data for various peridotitic systems and was found to be consistent within 50 °C and 0.4 GPa with petrographic constraints imposed by graphite and diamond stability (Nimis and Grütter, 2010). The Nickel and Green (1985) geobarometer was corrected according to Carswell (1991) for orthopyroxenes with molar Na > (Cr + Ti). *P–T* conditions were estimated by single-clinopyroxene geothermobarometry (Nimis and Taylor, 2000) for the four Zagadochnaya lherzolite microxenoliths, for which Ziberna et al. (2013) did not report orthopyroxene analyses. The single-clinopyroxene geothermometer produces results that are almost indistinguishable from those obtained with the Taylor (1998) geothermometer (Nimis and Grütter, 2010) and the single-clinopyroxene geobarometer shows good agreement with the Nickel and Green (1985) geobarometer in the *P* range of the Zagadochnaya samples (3.1–3.7 GPa; cf. Nimis et al., 2020). Therefore, these single-clinopyroxene thermobarometric estimates should not have introduced any particular bias in the dataset.

The following restrictions were adopted to ensure the most robust *P–T* estimates for all the xenoliths: weight percentage totals for pyroxenes and garnet 98.5–101.5, cations per six-oxygen formula unit in pyroxenes 3.99–4.02, $T > 700$ °C, $P > 1.5$ GPa. The slightly asymmetric safety interval for cation totals allows for the presence of some Fe^{3+}. Samples with documented disequilibrium among minerals were not considered. A further equilibrium check was made by comparing *P–T* estimates obtained using independent, internally consistent geothermobarometers. Samples for which the difference between calculated two-pyroxene (Taylor, 1998) and Ca-in-orthopyroxene (Brey and Köhler, 1990) temperatures (ΔT_{px}) were beyond their respective uncertainties and known systematic discrepancies (cf. Nimis and Grütter, 2010) were discarded. For this purpose, the Ca-in-orthopyroxene geothermometer was corrected as in Nimis and Grütter (2010) to ensure consistency with the Taylor (1998) geothermometer over the entire *T* range of interest. The adopted restrictions were $\Delta T_{px} < 90$ °C for $T_{Taylor1998} < 900$ °C, $\Delta T_{px} < 70$ °C for $T_{Taylor1998} = 900$–1200 °C, and $\Delta T_{px} < 50$ °C for $T_{Taylor1998} > 1200$ °C. These variable thresholds take into account the recognized decreasing precision of pyroxene geothermometry at lower *T* (cf. Nimis and Grütter, 2010). Note that the two-pyroxene geothermometer is almost entirely controlled by the clinopyroxene composition, whereas the Ca-in-orthopyroxene geothermometer is only controlled by the orthopyroxene composition. Therefore, the two methods provide independent *T* estimates. Since the Taylor (1998) geothermometer and the modified Ca-in-orthopyroxene geothermometer are internally consistent, these two geothermometers should provide similar results for well-equilibrated rocks. This important equilibrium check based on pyroxene compositions could only be made on peridotite xenoliths containing both clinopyroxene and orthopyroxene, thereby restricting the dataset to lherzolitic materials. A further equilibrium check was made by comparing *P* estimates using the Cr-in-clinopyroxene geobarometer (Nimis and Taylor, 2000; as corrected by Nimis et al., 2020) and the orthopyroxene–garnet geobarometer (Nickel and Green, 1985; as corrected by Carswell, 1991). Nimis et al.'s (2020) correction to the Cr-in-clinopyroxene geobarometer ensures that the two independent geobarometers are internally consistent. For two samples, the two *P* estimates diverged by >1 GPa, which is the maximum discrepancy observed in well-equilibrated mantle xenoliths (Nimis et al., 2020). This inconsistency suggests poor overall equilibrium and these samples were rejected. The latter equilibrium check could only be applied to samples with clinopyroxene compositions within the limits for robust single-clinopyroxene geobarometry (cf. Ziberna et al., 2016).

The above selection criteria consider chemical equilibria involving cations with different diffusivities (relatively high for divalent Ca and Mg in pyroxenes and low for trivalent Al and Cr in pyroxenes and garnets; e.g., Smith and Barron, 1991; Griffin et al., 1996; Cerniak and Dimanov, 2010). Therefore, a good match between independent *P–T* estimates should be a good indicator of overall equilibrium. The four Zagadochnaya microxenocrysts, for which orthopyroxene analyses are not available, were included in view of the good documented textural and geochemical equilibrium between garnet and clinopyroxene (Ziberna et al., 2013). These 4 samples, as well as other 20 samples for which only a partial equilibrium check could be performed, were accepted with reserve and will be considered separately. The final xenolith garnet dataset ($N = 119$) is reported in Table 1.

The on-craton xenoliths cover a wide range of *P–T* conditions, mostly lying between the 35- and 42-mW/m^2 conductive geotherms (Fig. 1). The off-craton xenoliths record hotter geothermal conditions and relatively low *P*. The marginal-craton samples from Namibia document a transition from typical cold cratonic conditions, recorded in coarse equant peridotites, to ca. 250 °C higher temperatures, recorded in mosaic-porphyroclastic peridotites, at roughly the same *P* of ~4 GPa. Thus, they form an array that lies at high-angle in *P–T* space relative to that of typical cratonic xenoliths (Fig. 1). In terms of CaO vs. Cr_2O_3

Table 2
Major element composition of minerals of samples from Pali Aike.

Sample	Mineral	SiO_2	TiO_2	Al_2O_3	Cr_2O_3	Fe_2O_3*	FeO	MnO	NiO	MgO	CaO	Na_2O	K_2O	Total	Si	Ti	Al	Cr	Fe^{3+}	Fe^{2+}	Mn	Ni	Mg	Ca	Na	K	Sum
LA10A	Ol	40.39	0.00	0.02	0.02		9.26	0.11	0.39	50.29	0.06	n.a.	n.a.	100.55	0.985	0.000	0.001	0.000		0.189	0.002	0.008	1.828	0.002			3.015
LA10A	Opx core	55.12	0.04	3.53	0.66		5.83	0.11	0.10	33.59	0.78	0.13	0.01	99.90	1.907	0.001	0.144	0.018		0.169	0.003	0.003	1.733	0.029	0.009	0.000	4.016
LA10A	Opx rim	55.29	0.04	3.67	0.72		5.82	0.15	0.10	33.78	0.79	0.14	0.01	100.50	1.904	0.001	0.149	0.017		0.168	0.004	0.003	1.734	0.029	0.010	0.000	4.018
LA10A	Cpx core	53.92	0.11	4.62	1.03		3.02	0.09	0.05	16.70	19.43	1.55	0.01	100.54	1.934	0.003	0.195	0.029		0.090	0.003	0.002	0.893	0.747	0.108	0.000	4.005
LA10A	Cpx rim	53.82	0.11	4.88	1.35		3.05	0.08	0.05	16.57	19.35	1.64	0.00	100.91	1.926	0.003	0.206	0.037		0.091	0.003	0.001	0.884	0.742	0.114	0.000	4.007
LA10A	Grt core	42.71	0.06	22.88	1.78		7.13	0.32	0.01	20.94	5.13	0.01	n.a.	100.98	2.996	0.003	1.892	0.099		0.418	0.019	0.000	2.190	0.386	0.001	0.000	8.006
LA10A	Spl in Grt	0.21	0.19	35.21	30.10	4.40	10.77	n.a.	0.25	17.31	n.a.	n.a.	n.a.	98.43	0.006	0.004	1.197	0.687	0.096	0.260		0.006	0.744				3.000
LA2	Ol	40.70	0.01	0.03	0.02		9.92	0.11	0.40	48.87	0.07	n.a.	n.a.	100.12	0.998	0.000	0.001	0.000		0.203	0.002	0.008	1.786	0.002			3.001
LA2	Opx core	54.45	0.12	3.64	0.55		6.12	0.11	0.11	33.13	0.81	0.17	n.a.	99.22	1.901	0.003	0.150	0.015		0.179	0.003	0.003	1.724	0.030	0.011		4.019
LA2	Opx rim	54.33	0.13	3.73	0.59		6.24	0.12	0.10	33.09	0.82	0.20	n.a.	99.35	1.897	0.004	0.153	0.014		0.182	0.003	0.003	1.722	0.031	0.014		4.023
LA2	Cpx core	52.60	0.41	5.32	1.27		3.27	0.08	0.05	15.94	18.57	2.02	0.00	99.53	1.911	0.011	0.228	0.037		0.099	0.003	0.001	0.863	0.723	0.142	0.000	4.017
LA2	Cpx rim	51.94	0.55	4.17	1.41		3.38	0.05	0.05	16.74	20.60	0.93	0.00	99.83	1.893	0.015	0.179	0.041		0.103	0.001	0.001	0.910	0.804	0.066	0.000	4.014
LA2	Grt core	41.96	0.15	22.46	1.49		7.67	0.32	0.01	20.92	4.94	0.01	n.a.	99.94	2.983	0.008	1.882	0.084		0.456	0.019	0.000	2.217	0.376	0.001	0.000	8.027
LA4	Ol	41.34	0.01	0.04	0.02		9.82	0.11	0.40	49.84	0.06	n.a.	n.a.	101.64	0.998	0.000	0.001	0.000		0.198	0.002	0.008	1.793	0.001			3.002
LA4	Opx core	55.25	0.14	3.71	0.64		6.33	0.11	0.11	33.51	0.81	0.15	n.a.	100.76	1.900	0.004	0.151	0.017		0.182	0.003	0.003	1.718	0.030	0.010		4.018
LA4	Cpx core	53.38	0.44	5.32	1.47		3.20	0.08	0.05	16.09	18.52	1.89	0.02	100.46	1.918	0.012	0.225	0.042		0.096	0.002	0.001	0.861	0.713	0.132	0.001	4.003
LA4	Cpx rim	53.56	0.44	5.50	1.37		3.24	0.08	0.05	16.14	18.53	1.98	0.01	100.89	1.916	0.012	0.232	0.038		0.097	0.002	0.001	0.860	0.710	0.137	0.001	4.006
LA4	Grt core	42.76	0.18	21.91	1.89		7.54	0.33	0.01	20.84	5.07	0.02	n.a.	100.56	3.021	0.010	1.824	0.105		0.446	0.019	0.000	2.195	0.384	0.003	0.000	8.007
TA28	Ol	40.35	0.01	0.03	0.01		10.47	0.11	0.39	48.62	0.06	n.a.	n.a.	100.05	0.993	0.000	0.001	0.000		0.216	0.002	0.008	1.784	0.002			3.006
TA28	Opx core	54.84	0.15	3.52	0.43		6.55	0.12	0.10	33.19	0.70	0.15	n.a.	99.74	1.906	0.004	0.144	0.012		0.190	0.003	0.003	1.719	0.026	0.010		4.018
TA28	Opx rim	55.03	0.15	3.86	0.42		6.55	0.12	0.10	33.29	0.79	0.17	n.a.	100.47	1.899	0.004	0.157	0.010		0.189	0.003	0.003	1.713	0.029	0.011		4.019
TA28	Cpx core	52.63	0.57	5.80	1.04		3.42	0.08	0.05	15.55	18.48	2.08	0.01	99.72	1.907	0.016	0.248	0.030		0.104	0.003	0.001	0.840	0.717	0.146	0.000	4.012
TA28	Cpx rim	52.68	0.59	5.83	1.02		3.55	0.08	0.05	15.62	18.52	1.99	0.00	99.94	1.905	0.016	0.249	0.029		0.107	0.003	0.001	0.842	0.718	0.140	0.000	4.010
TA28	Grt core	42.59	0.20	22.54	1.15		8.08	0.35	0.01	20.61	4.77	0.01	n.a.	100.32	3.013	0.011	1.879	0.065		0.478	0.021	0.000	2.174	0.362	0.002	0.000	8.005
TA28	Spl in Grt	0.22	0.83	38.32	25.21	4.87	11.90	0.07	0.30	17.32	n.a.	n.a.	n.a.	99.05	0.006	0.018	1.282	0.566	0.104	0.282	0.002	0.007	0.733				3.000
LA1	Ol	41.40	0.00	0.04	0.04		9.02	0.12	0.41	49.78	0.11	n.a.	n.a.	100.91	1.002	0.000	0.001	0.001		0.183	0.002	0.008	1.797	0.003			2.997
LA1	Opx core	54.43	0.06	3.95	0.87		5.56	0.12	0.14	33.08	1.03	0.14	n.a.	99.38	1.894	0.002	0.162	0.024		0.162	0.003	0.004	1.716	0.038	0.009		4.016
LA1	Opx rim	53.95	0.03	4.00	0.84		5.62	0.09	0.16	32.74	1.02	0.13	n.a.	98.60	1.893	0.001	0.166	0.023		0.165	0.003	0.005	1.713	0.038	0.009		4.016
LA1	Cpx core	52.80	0.11	4.92	1.57		3.05	0.09	0.06	16.86	18.94	1.42	0.01	99.83	1.911	0.003	0.210	0.045		0.092	0.003	0.002	0.910	0.734	0.100	0.000	4.009
LA1	Cpx rim	52.67	0.09	4.85	1.45		3.09	0.12	0.06	16.86	18.87	1.41	0.00	99.47	1.913	0.002	0.208	0.042		0.094	0.004	0.002	0.913	0.734	0.100	0.000	4.010
LA1	Grt core	42.15	0.04	21.35	3.13		6.91	0.34	0.01	20.13	5.80	0.01	n.a.	99.86	3.008	0.002	1.796	0.177		0.412	0.020	0.001	2.142	0.443	0.001	0.000	8.003
LA1	Spl in Grt	0.23	0.18	32.66	33.54	4.55	11.02	n.a.	0.21	17.15	n.a.	n.a.	n.a.	99.54	0.007	0.004	1.113	0.767	0.099	0.266		0.005	0.739				3.000
LA1	Spl ext. Grt	0.22	0.20	37.27	28.74	4.01	10.18	n.a.	0.29	18.00	n.a.	n.a.	n.a.	98.92	0.006	0.004	1.248	0.645	0.086	0.242		0.007	0.762				3.000
LA11	Ol	40.88	0.01	0.06	0.03		9.63	0.12	0.41	48.88	0.08	n.a.	n.a.	100.10	1.001	0.000	0.002	0.000		0.197	0.002	0.008	1.784	0.002			2.998
LA11	Opx core	54.68	0.11	3.62	0.64		5.90	0.12	0.11	33.25	0.81	0.14	n.a.	99.38	1.903	0.003	0.148	0.018		0.172	0.004	0.003	1.726	0.030	0.009		4.015
LA11	Opx rim	54.53	0.12	3.77	0.70		5.93	0.13	0.12	33.19	0.82	0.13	n.a.	99.44	1.898	0.003	0.155	0.019		0.173	0.004	0.003	1.722	0.030	0.009		4.016
LA11	Cpx core	52.84	0.30	4.83	1.37		3.09	0.08	0.05	16.31	19.19	1.57	0.01	99.64	1.917	0.008	0.207	0.039		0.094	0.002	0.001	0.882	0.746	0.111	0.000	4.007
LA11	Cpx rim	52.81	0.32	4.93	1.35		3.18	0.10	0.05	16.28	19.18	1.62	0.00	99.81	1.914	0.009	0.211	0.039		0.096	0.003	0.001	0.880	0.745	0.114	0.000	4.010
LA11	Grt core	42.16	0.15	21.77	1.92		7.52	0.33	0.01	20.26	5.18	0.03	n.a.	99.34	3.017	0.008	1.836	0.109		0.450	0.020	0.000	2.162	0.397	0.003	0.000	8.004

TiO_2, MnO, NiO and, for olivine, Cr_2O_3 by LA-ICP-MS, other oxides by EDS-WDS analysis (see text);
n.a.: not analyzed.
* : calculated by stoichiometry;

relationships, most of the on-craton and the marginal-craton garnets follow the typical lherzolitic trend (Fig. 2). The off-craton garnets have low Cr_2O_3 contents and slightly higher CaO than on-craton garnets with similar Cr_2O_3 contents (Fig. 2).

To further extend the *P*–*T* and compositional coverage, the xenolith dataset was integrated with data for garnets coexisting with olivine in high-*T*, high-*P* experiments at natural Ni abundances by Sudholz et al. (2021), using averages of compositions reported in their paper. These experiments were run for 120 h and the uniform Ni concentrations measured in the olivines and garnets by LA-ICP-MS suggest a close approach to equilibrium. In a *P*–*T* plot, these experiments would fall on relatively hot geotherms typical of off-craton mantle settings, but at higher *P*–*T* conditions than the off-craton xenoliths (Fig. 1). In the Cr_2O_3 vs. CaO plot, the experimental garnets show significant CaO variations, ranging from typical lherzolitic values to lower, 'harzburgitic' CaO contents, at relatively constant and moderate Cr_2O_3 contents (Fig. 2). We did not include other experimental data in the calibration dataset for reasons explained below.

Most of the experiments by Canil (1994) were run at enhanced Ni abundances. As illustrated by Canil (1999), the experiments with Ni_{Grt} > 3000 ppm were inconsistent with those run at similar *T* at natural Ni abundances, indicating deviations from Henry's law. The other Ni-doped experimental garnets did not reveal obvious discrepancies. However, considering the reported uncertainties, we believe it is difficult to define a safe limit for the compliance to Henry's law (cf. Fig. 4 in Canil, 1999). To avoid any possible bias, we decided not to include Canil's (1994) experiments at enhanced Ni abundances in the calibration database. Unfortunately, the reported uncertainties on Ni_{Grt} for the two experiments of Canil (1994) run on a natural peridotite composition are very large (ca. 90 ppm at the 1-σ confidence level) as compared to variations observed in Sudholz et al. (2021) experiments (σ for analyses on individual grains ≈ 20–40 ppm; grain-to-grain variations of average compositions in the same experiment = 2–8 ppm) and to the typical precision of proton microprobe and LA-ICP-MS analyses (± 2–10 ppm). Therefore, we did not include these two experiments in the calibration dataset, but we will still consider them for the validation of our geothermometer.

The experiments by Canil (1999) were run at natural Ni abundances, but some of the resulting reversal brackets are relatively wide as compared to the precision achievable with proton microprobe or LA-ICP-MS measurements and to the overall variations observed in xenoliths at any given *T* (Fig. 3). Therefore, we decided not to use these experiments for the geothermometer recalibration. Nonetheless, the reported experimental brackets and half-brackets provide useful independent constraints that will be used to validate our results.

Only partial data descriptions are available for the experiments by Yaxley and O'Neill (2008). These experiments were all Ni-doped, with NiO contents in olivine up to several wt%. For this reason, these experiments were not explored in further detail.

Other published experiments reporting low-precision Ni concentrations in garnet measured using routine electron microprobe analytical conditions were not considered.

3. Ni–*T*–*P* relationships in peridotitic garnets

The partitioning of Ni between garnet and olivine can be described by the distribution coefficient $D_{Ni} = Ni_{Grt}/Ni_{Ol}$ (ppm). The $\ln D_{Ni}$ vs. $1/T$ diagram provides a useful starting point to investigate the effects of *T* and *P* on D_{Ni}. High-precision Ni contents in the xenolith olivines were rarely reported. Therefore, a constant value of 2900 ppm was assumed, which corresponds to the average value for mantle olivines (mean ± standard deviation = 2900 ± 360 ppm, corresponding to 0.37 ± 0.05 wt % NiO; Ryan et al., 1996) and is within the limited range of values reported for olivine in Sudholz et al.'s (2021) experiments (ca. 2800–3200 ppm). The measured Ni contents in the Pali Aike olivines studied here (3059–3227 ppm) are also close to this value (Table 1). A similar procedure of assuming a fixed Ni_{Ol} value is normally used when the Ni-in-Grt geothermometer is applied to natural samples for which the Ni content in the associated olivine is unknown, such as garnet xenocrysts or garnet inclusions in diamonds. This practice is justified, because even large deviations of Ni_{Ol} from the average value cause only minor changes in the final *T* estimates, which remain largely controlled by Ni_{Grt}. If the effect of *P* is negligible and the behavior of Ni follows Henry's law, as expected from low Ni concentrations in the garnet, all data should plot on the same straight line, allowing for uncertainties. Such alignment is not observed for the calibrant dataset assembled for the current study (Fig. 3). At high *T* (> 950 °C), samples plotting on hot geotherms (i.e., the experiments and the off-craton xenoliths) have systematically higher D_{Ni} than those plotting on cold geotherms (i.e., the on-craton xenoliths). Most lower-*T* on-craton xenoliths, which record low *P* conditions similar to those in Sudholz et al.'s (2021) experiments, fall on the low-*T* extension of the experiment trend. Note that the off-craton and experimental garnets have variable CaO contents, the cratonic garnets have highly variable CaO and Cr_2O_3 contents (Fig. 2) unrelated to *T* or *P*, and the reported Ni contents in olivines are not systematically different between on-craton and off-craton xenoliths (mean ± standard deviation = 0.36 ± 0.06 wt% and 0.37 ± 0.04 wt% NiO, respectively; Table 1). Therefore, the two contrasting trends cannot be ascribed to compositional effects. It is also noteworthy that the displacement of on-craton xenoliths in the $\ln D_{Ni}$ vs. $1/T$ plot is not restricted to samples on which only a partial equilibrium check could be performed, due to a lack of $T_{Ca\text{-in-orthopyroxene}}$ or $P_{Cr\text{-in-clinopyroxene}}$ estimates (Fig. 3). Therefore, the two contrasting trends are unlikely to be an artifact related to xenolith disequilibrium.

The data shown in Fig. 3 indicate that either two-pyroxene *T* estimates for most cratonic xenoliths are overestimated by ~100–200 °C or *P* has a non-negligible effect on Ni partitioning. Canil (1996), in his reply to Griffin and Ryan's (1996) discussion, suggested that inconsistencies between experimental and empirical calibrations of the Ni-in-Grt geothermometer were due to thermobarometric uncertainties and consequent inconsistent *P* corrections to temperature estimates rather than to real *P* effects. Owing to the small *P* dependence of the two-pyroxene

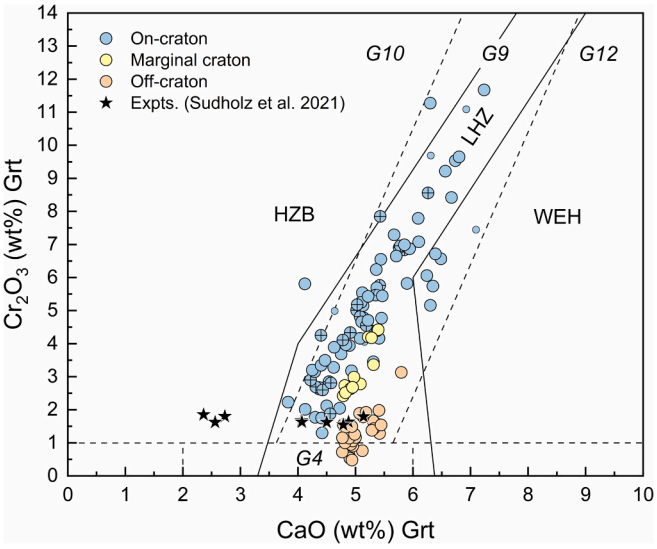

Fig. 2. Cr_2O_3 vs. CaO relationships in garnets used for the recalibration of the Ni-in-Grt geothermometer. Crossed circles indicate samples for which only a partial equilibrium check could be performed (see text). Small circles indicate samples that were outliers in the $\ln D_{Ni}$ vs. reciprocal *T* plot (cf. Fig. 3) and were not used for the geothermometer recalibration. Compositional boundaries for garnets in harzburgite (HZB), lherzolite (LHZ) and wehrlite (WEH) assemblages (solid lines) are from Sobolev et al. (1973). Compositional boundaries for G4 (pyroxenitic), G9 (lherzolitic), G10 (harzburgitic) and G12 (wehrlitic) garnets (dashed lines) are from Grütter et al. (2004).

thermometer used here (25–45 °C/GPa), an enormous overestimation of P for most cratonic xenoliths of ~4 GPa would be necessary, however, to account for the observed discrepancies. This hypothesis is challenged by cross-validation of independent thermobarometric estimates (see above), and by the fact that all samples plot, as expected, on geologically reasonable conductive geotherms (Fig. 1).

A further possibility to be considered is that different chemical equilibria among minerals, which involve elements with different diffusivities, could record different apparent temperatures during late thermal perturbations in the mantle or after incorporation of the xenoliths in the hot kimberlite magmas. Although Ni diffusivity in garnet is probably higher than Ca–Mg diffusivity in pyroxenes, xenoliths containing strongly zoned garnets typically lack pronounced zoning for Ni in garnets and for Ca–Mg in pyroxenes (Griffin et al., 1996). This suggests that mechanisms other than volume diffusion are involved in pyroxene reequilibration and that all these T-sensitive elements reequilibrate rapidly during mantle processes (Griffin et al., 1996). Therefore, Ni-in-garnet and pyroxene temperature estimates are unlikely to be decoupled. Even if volume diffusion was the dominant mechanism, one would rather expect thermally perturbed xenoliths to show Ni temperatures *in excess* of two-pyroxene temperatures and thus fall *to the right* of the experiment trend in Fig. 3. Accordingly, short-lived heating might possibly account for the evident outliers plotting to the right of the main trend, but not for the bulk of the cratonic xenoliths falling to its left. The hypothesis of a significant P dependence of Ni partitioning thus remains the most likely.

The observed Ni_{Grt}–T–P relationships can be described by a P-dependent geothermometer:

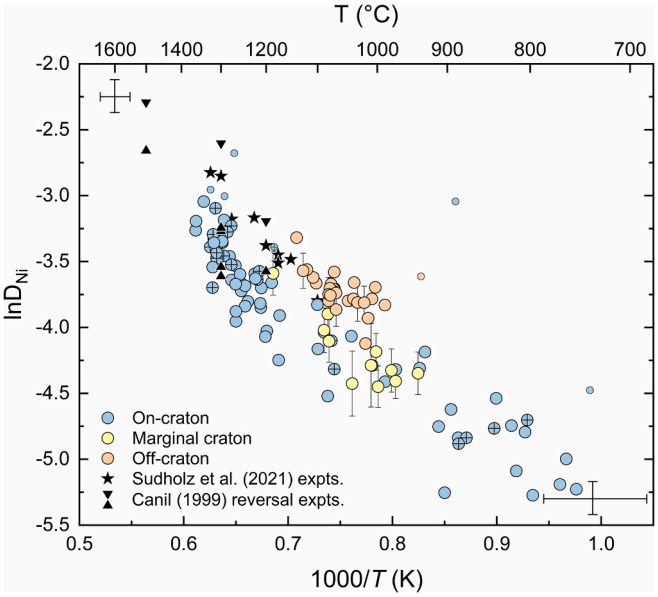

Fig. 3. Relationships between $\ln(Ni_{Grt}/Ni_{Ol})$ and reciprocal T in the calibration dataset. Ni content in the xenolith olivines is assumed to be 2900 ppm. Crossed circles indicate samples for which only a partial equilibrium check could be performed (see text). Small symbols indicate outliers that were not considered for the geothermometer calibration. Representative error bars for the xenoliths are shown at the two ends of the data array. Errors on T are assumed to be ±50 °C, considering uncertainties of the Taylor (1998) geothermometer (SEE = 31 °C) and propagation of analytical and P uncertainties (Nimis and Grütter, 2010). Errors on $\ln D_{Ni}$ were calculated by normal error propagation, assuming a relative uncertainty on Ni_{Grt} measurements of 5% and an uncertainty on Ni_{Ol} of 360 ppm, corresponding to the standard deviation of olivine compositions in mantle xenoliths (Ryan et al., 1996). In this calculation, the contribution of Ni_{Ol} uncertainties is by far the most important. Error bars on symbols used real standard deviations on Ni_{Grt} analyzed in this work. Experimental brackets and half-brackets after Canil (1999) at 3–7 GPa are shown for comparison.

$$T\ (\mathrm{K}) = \frac{7451 + 243.6 \cdot P(\mathrm{GPa})}{2.31 - ln\frac{Ni_{Grt}\ (ppm)}{Ni_{Ol}\ (ppm)}}. \quad (2)$$

This expression was obtained by regression after excluding seven outliers (indicated by smaller symbols in Fig. 3). Ni_{Ol} was assumed to be 2900 ppm for all the xenoliths, so as to reduce the impact of poor precision olivine analyses and to match conditions typically encountered in single-garnet thermobarometric applications. Expression (2) reproduces the calibration T with a standard error of estimate (SEE) of 44 °C, with no systematic deviations with changing P, CaO_{Grt} or Cr_2O_{3Grt} (Fig. 4–5). The P dependence (ca. 40 °C/GPa) is comparable to that of the olivine–garnet Fe–Mg exchange geothermometer (ca. 50 °C/GPa; Wu and Zhao, 2007). Although Canil's (1999) experiments were not included in the calibration, the new geothermometer is consistent with his experimental brackets at 3–7 GPa and 1200–1500 °C (Fig. 6). Temperatures for Canil's (1994) experiments at natural Ni abundances at 1600–1700 °C and 5 GPa are also reproduced within their experimental errors, while those at enhanced Ni abundances show systematic T overestimation (Fig. 6), suggesting deviations from Henry's law.

Attempts to calibrate the geothermometer using real Ni_{Ol} data, mostly based on low-precision electron microprobe analyses, produced larger residuals and were abandoned. The effect of assuming a fixed Ni_{Ol} = 2900 ppm is illustrated in Fig. 7 for the few xenoliths for which precise Ni_{Ol} data are available. The differences between T estimates calculated using real and fixed Ni_{Ol} values are mostly within ±1 SEE of the geothermometer calibration. Much larger errors may only occur for samples with unusually high or unusually low Ni_{Ol}.

Thanks to the incorporation of a P term, Eq. (2) can be applied to both on-craton and off-craton peridotitic garnets that are buffered for Ni content by coexisting olivine. Conversely, none of the previous formulations of the Ni-in-Grt geothermometer satisfactorily reproduce T for the whole dataset (Fig. 4). Unfortunately, a P-dependent Ni-in-Grt geothermometer may not be practical, because an independent estimate of P is rarely available for single-garnet geothermometry. Possible favorable cases are those in which P can be derived by projection onto a model geotherm (Nimis, 2022; Ryan et al., 1996) or inclusions in diamonds for which P is estimated by elastic barometry (Angel et al., 2022). Attempts to calibrate the geothermometer by considering only the cratonic garnets still evidenced a significant P dependence, despite the reduced P range at any given T in the calibration data. In principle, it should be possible to derive a P-independent geothermometric formulation if P is a function of T, as it is the case for samples equilibrated along a known or specified geotherm. According to modern models, mantle conductive geotherms are close to linear in P–T space for a given surface heat flow (Hasterok and Chapman, 2011). To extend the applicability of the Ni-in-Grt method, simplified P-independent geothermometers have been formulated for reference geotherms specified by Hasterok and Chapman (2011), by modelling P as linear functions of T in the relevant P–T ranges:

$$T_{35}\ (\mathrm{K}) = \frac{6452}{0.451 - ln\frac{Ni_{Grt}\ (ppm)}{2900}} \quad (3)$$

$$T_{40}\ (\mathrm{K}) = \frac{6735}{0.955 - ln\frac{Ni_{Grt}\ (ppm)}{2900}} \quad (4)$$

$$T_{45}\ (\mathrm{K}) = \frac{6889}{1.25 - ln\frac{Ni_{Grt}\ (ppm)}{2900}} \quad (5)$$

$$T_{50}\ (\mathrm{K}) = \frac{7197}{1.52 - ln\frac{Ni_{Grt}\ (ppm)}{2900}} \quad (6)$$

$$T_{60}\ (\mathrm{K}) = \frac{7099}{1.67 - ln\frac{Ni_{Grt}\ (ppm)}{2900}} \quad (7)$$

where the subscripts 35, 40, 45, 50 and 60 indicate the surface heat flow (mW/m^2) for the reference model geotherms.

These simplified formulations permit traditional application of the Ni-in-Grt geothermometer as a single-mineral method, provided an initial estimate of the local geothermal conditions has been made. Eqs. (3) and (4) will bracket conductive conditions for most cratonic garnets. Eqs. (4) and (5) will bracket conditions for most marginal-craton garnets. Eqs. (5) through (7) will cover conditions for most off-craton garnets.

Fig. 8 shows the performance of formulation T_{60} on the off-craton garnets, which last equilibrated close to a 60-mW/m^2 conductive geotherm, and of formulation T_{40} on garnets from the Kaapvaal craton and the low-T (<1080 °C) garnets from Namibia, which last equilibrated close to a 40-mW/m^2 conductive geotherm. T_{60} reproduces the pyroxene temperatures for the 27 off-craton garnets within ±70 °C (SEE = 35 °C), very similar to the full P-dependent formulation (±58 °C and SEE = 32 °C for the same samples). T_{40} reproduces the pyroxene temperatures for the 28 Kaapvaal–Namibian cratonic garnets within ±125 °C (SEE =

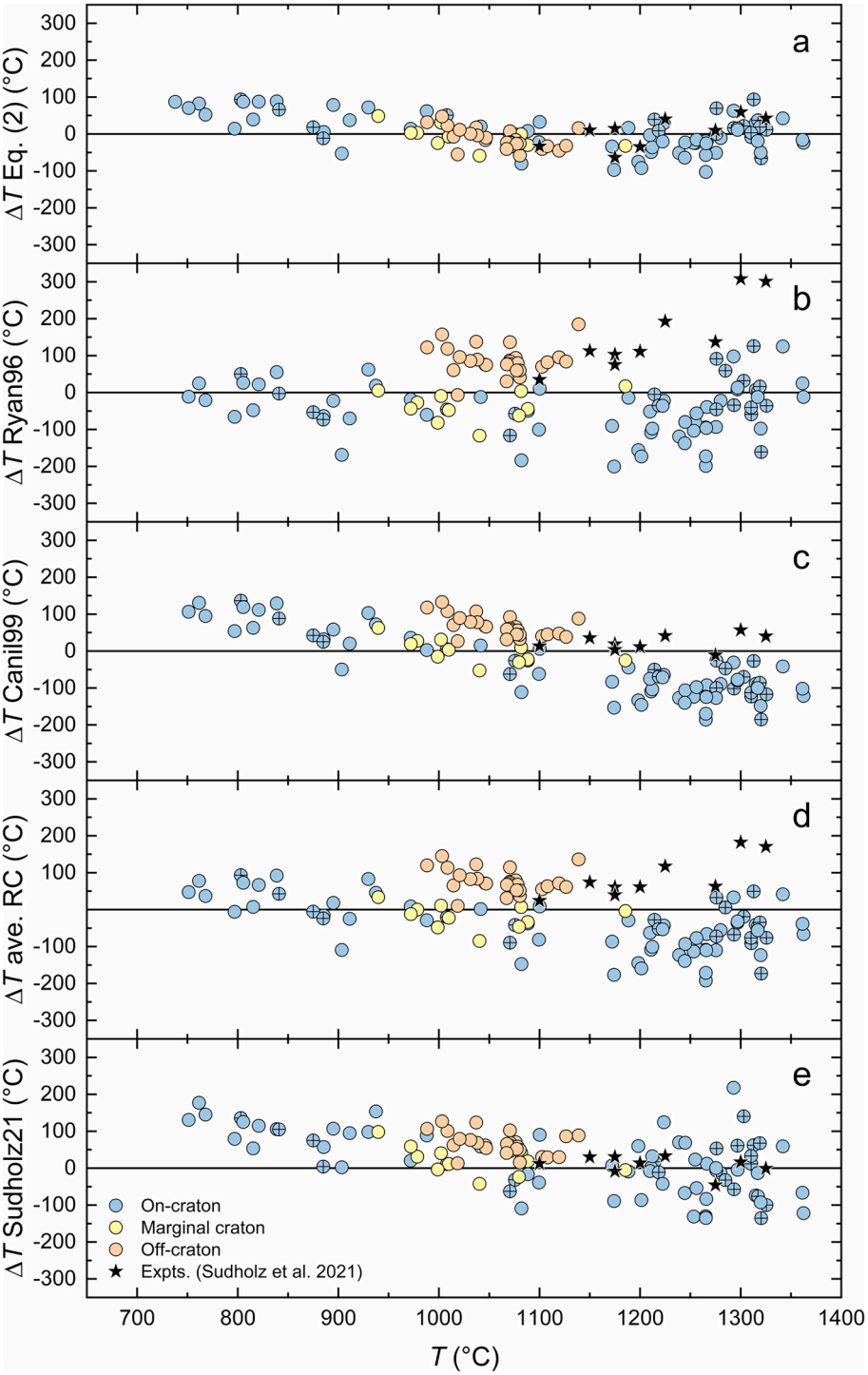

Fig. 4. Differences between temperatures calculated using different versions of the Ni-in-Grt geothermometer and nominal temperatures for the calibration dataset. *Ave. RC* is the average of T estimates obtained using the Ryan et al. (1996) and Canil (1999) geothermometers. Eq. (2) is from this work. Crossed circles indicate samples for which only a partial equilibrium check could be performed (see text).

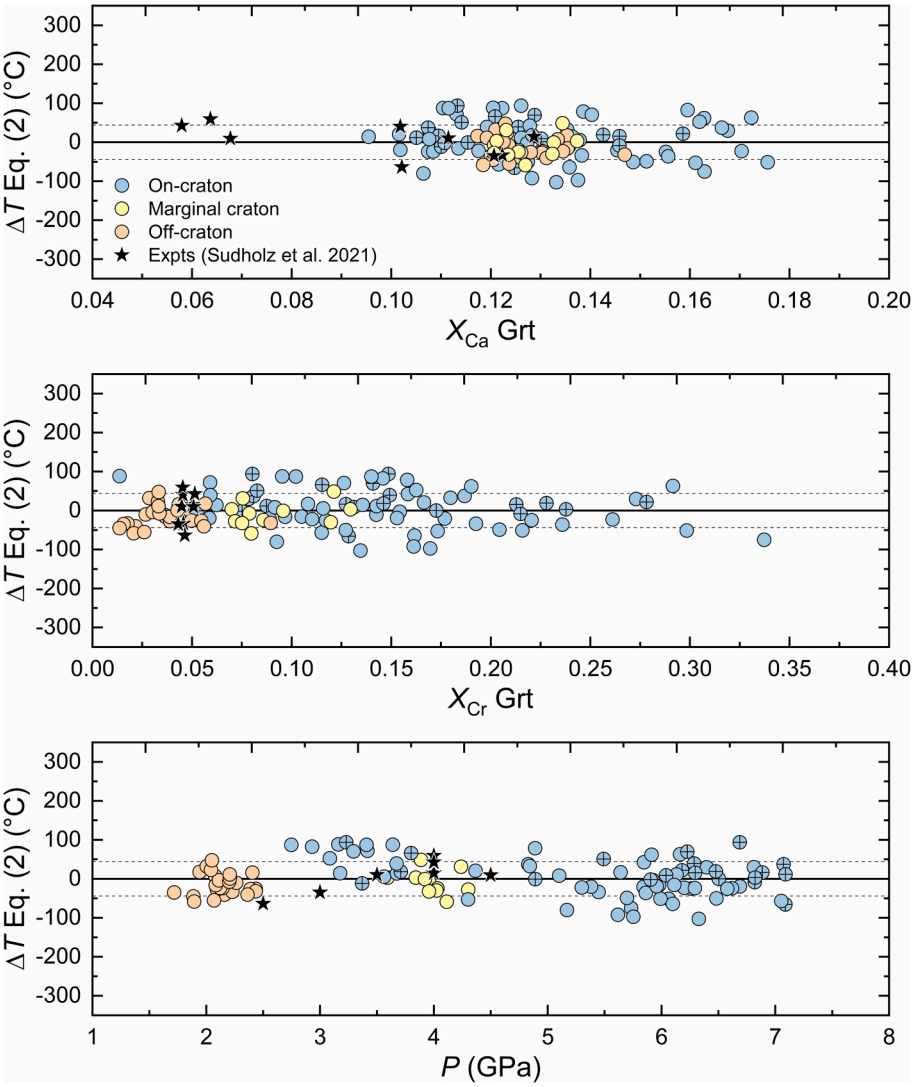

Fig. 5. Differences between calculated and nominal temperatures using the new *P*-dependent Ni-in-Grt calibration against *P* and garnet X_{Ca} and X_{Cr}. Dashed lines are at ±SEE. Crossed circles indicate samples for which only a partial equilibrium check could be performed (see text).

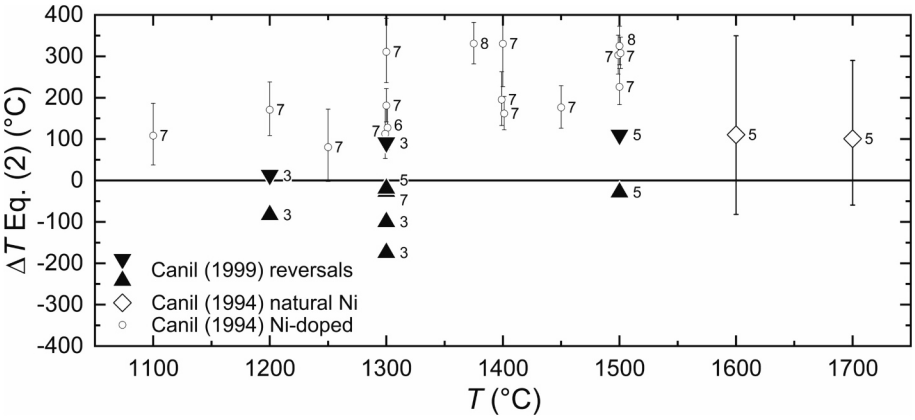

Fig. 6. Differences between calculated and nominal temperatures using the new *P*-dependent Ni-in-Grt calibration for Canil's (1999) reversal experiments at natural Ni abundance and Canil's (1994) experiments at enhanced and natural Ni abundance. Triangles pointing downward and upward represent the reversal bracket for Ni-rich garnet seeds and natural Ni-poor garnets, respectively. Labels indicate the experimental *P* (GPa). Some of Canil's (1994) data have been displaced a few degrees from their actual temperatures to avoid overlaps of error bars.

51 °C), that is somewhat worse than the full *P*-dependent formulation (±88 °C, SEE = 37 °C for the same samples). In this case, the three records with residuals greater than ±70 °C are the same that had residuals greater than ±70 °C also in the *P*-dependent calibration, suggesting minor disequilibrium or analytical issues in the original data. If these three records are excluded, the T_{40} residuals become ±69 °C and the SEE is reduced to 37 °C.

4. Discussion

Although effective ionic radii for Ni and Mg in silicates are usually much more similar than those for Mg and Fe, the very different crystal-field stabilization energies between six-fold-coordinated Ni in olivine and eight-fold-coordinated Ni in garnet cause the molar volume of endmember Ni-garnet to be significantly larger than that of pyrope Mg-garnet (Ross II et al., 1996; Table 3). Consequently, the ΔV°_{298} for the Mg–Ni-exchange reaction (1) is not negligible and is even larger than that of the homologous Fe–Mg-exchange reaction (Table 3). Thus, the Ni partitioning between garnet and olivine is predictably *P*-dependent. The different trends constrained in this study for on-craton and off-craton mantle garnets in the $\ln D_{Ni}$ vs. $1/T$ diagram confirm this prediction (Fig. 3). The recognition of a non-negligible *P* effect on Ni partitioning allows an easy explanation for the discrepancies observed using previous formulations of the Ni-in-Grt geothermometer and a solution to the long-standing controversy as to which Ni-in-Grt geothermometer is best (cf. Canil, 1996, 1999; Griffin and Ryan, 1996).

The Ryan et al. (1996) geothermometer was calibrated on a large suite of mantle xenoliths spanning various geotherms. The absence of marked systematic deviations at high or low *T* (Fig. 4b) is not surprising, since the calibration dataset had a good statistical leverage in *P*–*T* space. Nonetheless, the lack of a *P* term led to systematic *T* overestimation for samples on hot geotherms (including the experiments) and *T* underestimation for most of those on cold geotherms. This is particularly relevant for the high-*T* samples, because the *P* effect increases with increasing *T*. The use of non-robust geothermobarometer combinations to estimate the xenolith *P*–*T* probably also contributed to impair the precision of the Ryan et al. (1996) geothermometer.

The Canil (1999) geothermometer was calibrated on experiments at very high *T* (1200–2040 °C), including new reversals at 1200–1500 °C and five previous melting experiments on a natural peridotite at 1600–2040 °C by Canil (1994) and Herzberg and Zhang (1996). Most of these experiments would plot on hot model conductive geotherms (Fig. 1). The Canil (1999) calibration superseded an earlier experimental calibration by the same author that used non-natural, Ni-doped compositions (Canil, 1994). Experimental control on input *T* values afforded higher precision relative to Ryan et al.'s (1996) calibration. Nonetheless, the absence of a *P* term again introduced systematic deviations (Fig. 4c). The evident *T* overestimation at low *T* (low *P*) and *T* underestimation at high *T* (high *P*) that is observed for samples plotting on cold geotherms is interpreted here to be a compensation effect due to the inability of the Canil (1999) regression to properly make up for the *P* influence. This effect is further enhanced by the large extrapolation to low *T*. Unsurprisingly, Sudholz et al.'s (2021) experiments, which were run at high *T* and at *P*/*T* ratios similar to those of most of the experiments used for Canil's (1999) calibration (Fig. 1), are reproduced very well (Fig. 4c). Canil (1994, 1999) reasonably used the simplest possible thermometric expression for his calibrations, based on evidence available at that time. Unfortunately, *P* effects remained within the uncertainties of the calibration experiments and were thus overlooked.

Some workers have suggested that the average of $T_{\text{Ryan et al. (1996)}}$ and $T_{\text{Canil (1999)}}$ could provide more robust *T* estimates than either geothermometers in real-world applications (Czas et al., 2020; Nimis et al., 2020). In fact, the average protocol dampens the large uncertainties of the Ryan et al. (1996) thermometer but, obviously, it does not make up for the *P* effects (Fig. 4d).

The Sudholz et al. (2021) geothermometer provides minor overall improvement at high-*T* relative to the Canil (1999) geothermometer, but at the expense of poorer precision (Fig. 4e). This is again unsurprising, since *P* effects were assumed negligible and poorly constrained correction parameters for Ca_{Grt} and Cr_{Grt} were included in the geothermometer formulation. Indeed, the calibration dataset covered a Cr_{Grt} range (Fig. 2) that was too small to derive any meaningful correction parameter for Cr_{Grt} by data regression. Moreover, since Ca_{Grt} and Cr_{Grt} showed

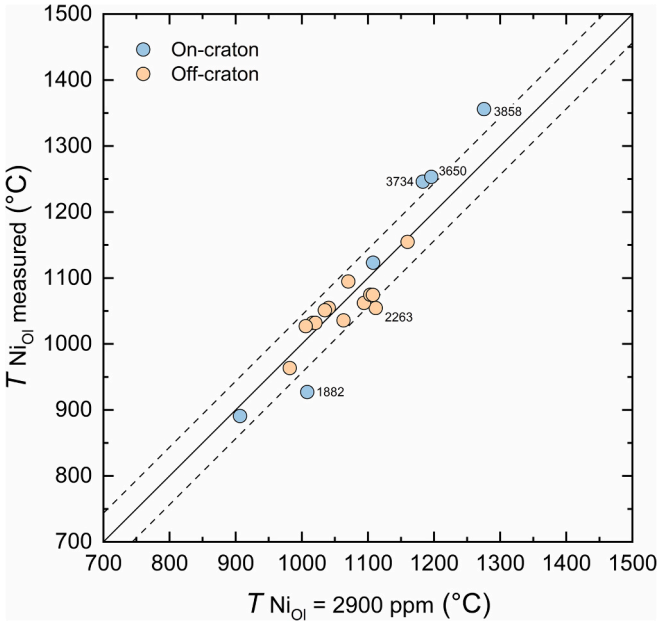

Fig. 7. Comparison between Ni-in-Grt temperatures calculated with Eq. (2) using real Ni_{Ol} concentrations vs. assuming a fixed Ni_{Ol} = 2900 ppm. Dashed lines are at ±1 SEE of the geothermometer calibration. Labels indicate real Ni_{Ol} values for samples showing the largest discrepancies. The other samples have Ni_{Ol} in the range 2517–3227 ppm.

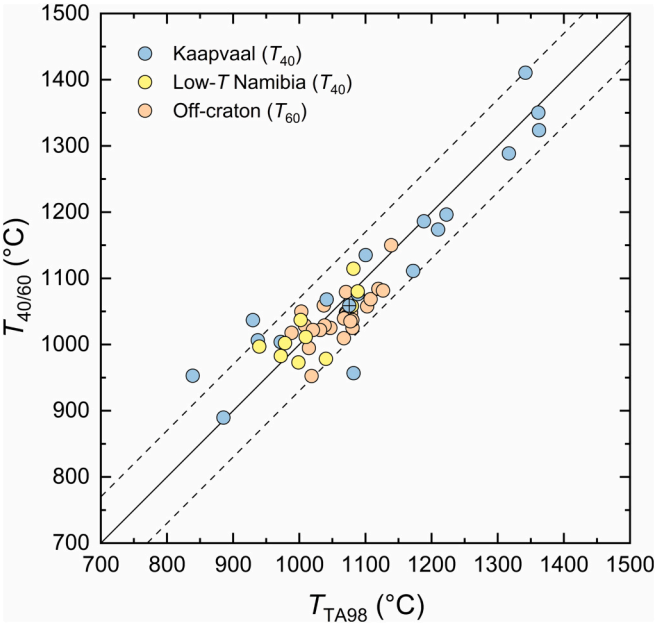

Fig. 8. Comparison between calibrant pyroxene-thermometry results and *T* estimates using the new geotherm-referenced T_{40} formulation for Kaapvaal and low-T Namibian calibrant garnet compositions and the T_{60} formulation for off-craton calibrant garnet compositions. Dashed lines are at ±70 °C. Crossed circles indicate samples for which only a partial equilibrium check could be performed (see text).

Table 3
Molar volumes for garnet and olivine endmembers and calculated ΔV°_{298} for relevant exchange reactions.

Mineral	Endmember	V°_{298} (J/bar)	Reference
Garnet	Pyrope	11.313	Holland and Powell (2011)
	$(Mg_{0.82}Ni_{0.18})_3Al_2Si_3O_{12}$	11.357	Canil (1994)
	$Ni_3Al_2Si_3O_{12}$	11.557	*
	Almandine	11.525	Holland and Powell (2011)
Olivine	Forsterite	4.366	Holland and Powell (2011)
	Ni_2SiO_4	4.259	Hirschmann (1991)
	Fayalite	4.631	Holland and Powell (2011)
$\frac{1}{3}Mg_3Al_2Si_3O_{12} + \frac{1}{2}Ni_2SiO_4 = \frac{1}{3}Ni_3Al_2Si_3O_{12} + \frac{1}{2}Mg_2SiO_4$			$\Delta V^{\circ}_{298} = 0.13$ J/bar
$\frac{1}{3}Fe_3Al_2Si_3O_{12} + \frac{1}{2}Mg_2SiO_4 = \frac{1}{3}Mg_3Al_2Si_3O_{12} + \frac{1}{2}Fe_2SiO_4$			$\Delta V^{\circ}_{298} = 0.06$ J/bar

* : Calculated by linear extrapolation assuming ideal behavior (cf. Canil, 1994).

weak negative and, respectively, positive correlations with *P* in Sudholz et al.'s (2021) experiments, the Ca and Cr correction terms most likely functioned as poor substitutes for the missing *P* term. Thus, although the introduction of additional regression parameters obviously improved regression statistics, probably this was mostly by regressing noise and led to overfitting (Pardoe, 2021). The poorly constrained corrections in fact reduced the predictive power of the regression outside the compositional space of the calibration, as evidenced by strongly increased *T* residuals for occasional samples at high *T* (Fig. 4e).

The new *P*-dependent geothermometer (Eq. (2)) reproduces the nominal *T* for our compiled xenolith and experimental dataset with much better accuracy and precision than any of the calibrations discussed above (Fig. 4f). The lack of correlation between *T* residuals and garnet compositional parameters (Fig. 5) confirms that compositional effects are negligible. Only small systematic, progressive overestimation still occurs at $T < 900$ °C (up to ca. +75 °C at 700 °C). It is unclear whether this residual inconsistency is due to inaccuracy of the reference pyroxene geothermometers, which are poorly constrained below 900 °C (Nimis and Grütter, 2010), of the Ni-in-Grt geothermometer or of both. Potential errors nevertheless remain within reasonable limits for most applications.

Similar to previous calibrations, changing the value of Ni_{Ol} generally produces only minor changes in the calculated *T*. Increasing or decreasing Ni_{Ol} by 500 ppm would decrease or, respectively, increase *T* by ca. 25 °C at 800 °C to ca. 55 °C at 1400 °C. Considering the standard deviation for Ni in mantle olivine of 360 ppm (Ryan et al., 1996), errors due to the constant-Ni_{Ol} approximation will most often remain within the intrinsic uncertainty of the method.

The simplified geotherm-referenced geothermometer formulations (Eqs. (3)–(7)) may be less accurate than the full *P*-dependent expression (Eq. (2)), which should generally be preferred if an independent estimate of *P* is available. This is not normally the case for garnet xenocrysts from previously unexplored localities. When studying large xenocryst populations, Eqs. (3)–(7) may provide useful preliminary indications of *T* distribution, provided a local geotherm can be estimated. The actual geotherm may be determined in an iterative fashion, by using the *P*-dependent Eq. (2) in combination with the Cr-in-Grt minimum-*P* geobarometer (Ryan et al., 1996) or the Cr/Ca-in-garnet minimum-*P* geobarometer (Grütter et al., 2006), and the maximum-*P* envelope approach of Ryan et al. (1996). Note that Grütter et al.'s (2006) geobarometer also makes provision for different reference geotherms, in a manner similar to Eqs. (3)–(7) of this work.

5. Conclusions

In contrast with previous assumptions, the partitioning of Ni between mantle olivine and garnet is significantly *P*-dependent. Therefore, previous *P*-independent calibrations of the Ni-in-Grt geothermometer fail to correctly estimate *T* for many peridotitic Cr-pyrope garnets. Potential errors may exceed 150 °C. A *P*-dependent recalibration of the Ni-in-Grt geothermometer allows to estimate *T* for both on-craton and off-craton mantle garnets with a SEE of 44 °C. The recalibrated geothermometer is consistent with previous experiments on Ni partitioning between garnet and olivine at natural Ni abundances and markedly improves the consistency between Ni-in-Grt and pyroxene temperatures in applications to natural samples.

Simplified geotherm-referenced geothermometric formulations can be used for garnets equilibrated on known, estimated or assumed geotherms. These geotherm-referenced formulations permit traditional use of the Ni-in-Grt method as a single-mineral geothermometer, provided a local geotherm has been defined or, at least, inferred. Further refinement of both thermobarometric estimates and geothermal conditions can be achieved through a trial and error procedure, which involves iterative geotherm re-estimation in combination with the Cr-in-Grt minimum-*P* geobarometer (Ryan et al., 1996) or the Cr/Ca-in-garnet minimum-*P* geobarometer (Grütter et al., 2006). As it is always the case with single-garnet geothermobarometry, projecting a garnet *T* onto the estimated geotherm may lead to *P* overcorrections if the garnet last equilibrated at *T* higher than the local conductive geotherm, a condition that is fairly common for cratonic peridotites near the lithosphere base.

Declaration of competing interest

The authors declare that they have no known competing financial interests or personal relationships that could have appeared to influence the work reported in this paper.

Acknowledgements

The authors are deeply indebted to several generations of experimental and mantle petrologists, without whose work the present research could not be made. We are thankful to Karen Smit and Dmitri Ionov for allowing use of unpublished data. Reviews by H. Grütter, D. Canil and an anonymous reviewer helped us significantly improve our manuscript. The financial support of Università di Padova (DOR funds) and of the Italian "Programma di Rilevante Interesse Nazionale" project MUR PRIN_20178LPCPW is acknowledged. The Pali Aike samples were collected by G. Rivalenti and M. Mazzucchelli (University of Modena, Italy), R. Vannucci (University of Pavia, IGG-CNR Pavia, Italy) and C. Cingolani (University of La Plata, Argentina) during expeditions financially supported by MURST (COFIN 1998 and 2000), CNR and CNR-CONICET joint programs.

References

Agashev, A., Ionov, D., Pokhilenko, N., Golovin, A., Cherepanova, Y., Sharygin, I., 2013. Metasomatism in lithospheric mantle roots: constraints from whole-rock and mineral chemical composition of deformed peridotite xenoliths from kimberlite pipe Udachnaya. Lithos 160, 201–215. https://doi.org/10.1016/j.lithos.2012.11.014.

Angel, R.J., Alvaro, M., Nestola, F., 2022. Crystallographic methods for non-destructive characterization of mineral inclusions in diamonds. Rev. Mineral. Geochem. 88, 257–306. https://doi.org/10.2138/rmg.2022.88.05.

Ashchepkov, I.V., Ntaflos, T., Spetsius, Z.V., Salikhov, R.F., Downes, H., 2017. Interaction between protokimberlite melts and mantle lithosphere: evidence from mantle xenoliths from the Dalnyaya kimberlite pipe, Yakutia (Russia). Geosci. Front. 8, 693–710. https://doi.org/10.1016/j.gsf.2016.05.008.

Brey, G.P., Köhler, T., 1990. Geothermobarometry in four-phase lherzolites. II. New thermobarometers, and practical assessment of existing thermobarometers. J. Petrol. 31, 1353–1378. https://doi.org/10.1093/petrology/31.6.1353.

Canil, D., 1994. An experimental calibration of the `Ni in garnet' geothermometer with applications. Contrib. Mineral. Petrol. 117, 410–420. https://doi.org/10.1007/BF00307274.

Canil, D., 1996. An experimental calibration of the nickel in garnet geothermometer with applications: reply. Contrib. Mineral. Petrol. 124, 219–223. https://doi.org/10.1007/s004100050187.

Canil, D., 1999. The Ni-in-garnet geothermometer: calibration at natural abundances. Contrib. Mineral. Petrol. 136, 240–246. https://doi.org/10.1007/s004100050535.

Carswell, D.A., 1991. The garnet–orthopyroxene Al barometer: problematic application to natural garnet lherzolite assemblages. Mineral. Mag. 55, 19–31. https://doi.org/10.1180/minmag.1991.055.378.03.

Cerniak, D.J., Dimanov, A., 2010. Diffusion in pyroxene, mica and amphibole. Rev. Mineral. Geochem. 72, 641–690. https://doi.org/10.2138/rmg.2010.72.14.

Creighton, S., Stachel, T., Eichenberg, D., Luth, R.W., 2010. Oxidation state of the lithospheric mantle beneath Diavik diamond mine, central Slave craton, NWT, Canada. Contrib. Mineral. Petrol. 159, 645–657. https://doi.org/10.1007/s00410-009-0446-x.

Czas, J., Pearson, D.G., Stachel, T., Kjarsgaard, B.A., Read, G.H., 2020. A Palaeoproterozoic diamond-bearing lithospheric mantle root beneath the Archean Sask Craton, Canada. Lithos 356–357, 105301. https://doi.org/10.1016/j.lithos.2019.105301.

Davies, R.M., Griffin, W.L., O'Reilly, S.Y., Doyle, B.J., 2004. Mineral inclusions and geochemical characteristics of microdiamonds from the DO27, A154, A21, A418, DO18, DD17 and Ranch Lake kimberlites at Lac de Gras, Slave Craton, Canada. Lithos 77, 39–55. https://doi.org/10.1016/j.lithos.2004.04.016.

De Hoog, J.C.M., Stachel, T., Harris, J.W., 2019. Trace-element geochemistry of diamond-hosted olivine inclusions from the Akwatia Mine, West African Craton: implications for diamond paragenesis and geothermobarometry. Contrib. Mineral. Petrol. 174, 100. https://doi.org/10.1007/s00410-019-1634-y.

Franz, L., Brey, G., Okrusch, M., 1996. Steady state geotherm, thermal disturbances, and tectonic development of the lower lithosphere underneath the Gibeon Kimberlite Province, Namibia. Contrib. Mineral. Petrol. 126, 181–198. https://doi.org/10.1007/s004100050243.

Gibson, S.A., Malarkey, J., Day, J.A., 2008. Melt depletion and enrichment beneath the western Kaapvaal Craton: evidence from Finsch peridotite xenoliths. J. Petrol. 49, 1817–1852. https://doi.org/10.1093/petrology/egn048.

Glaser, S.M., Foley, S.F., Günther, D., 1999. Trace element compositions of minerals in garnet and spinel peridotite xenoliths from the Vitim volcanic field, Transbaikalia, eastern Siberia. Lithos 48, 263–285. https://doi.org/10.1016/S0024-4937(99)00032-8.

Grégoire, M., Bell, D., Le Roex, A., 2003. Garnet lherzolites from the Kaapvaal Craton (South Africa): trace element evidence for a metasomatic history. J. Petrol. 44, 629–657. https://doi.org/10.1093/petrology/44.4.629.

Griffin, W.L., Ryan, C.G., 1996. An experimental calibration of the "nickel in garnet" geothermometer with applications, by D. Canil: discussion. Contrib. Mineral. Petrol. 124, 216–218. https://doi.org/10.1007/s004100050186.

Griffin, W.L., Cousens, D.R., Ryan, C.G., Sic, S.H., Suter, G.F., 1989. Ni in chrome garnet: a new geothermometer. Contrib. Mineral. Petrol. 103, 199–202. https://doi.org/10.1007/BF00378505.

Griffin, W.L., Gurney, J.J., Ryan, C.G., 1992. Variations in trapping temperatures and trace elements in peridotite suite inclusions from African diamonds: evidence for two inclusion suites, and implications for lithosphere stratigraphy. Contrib. Mineral. Petrol. 110, 1–15. https://doi.org/10.1007/BF00310878.

Griffin, W.L., Sobolev, N.V., Ryan, C.G., Pokhilenko, N.P., Win, T.T., Yefimova, E.S., 1993. Trace elements in garnets and chromites: diamond formation in the Siberian lithosphere. Lithos 29, 235–256. https://doi.org/10.1016/0024-4937(93)90019-9.

Griffin, W.L., Smith, D., Ryan, C.G., O'Reilly, S.Y., Win, T.T., 1996. Trace element zoning in mantle minerals: metasomatism and thermal events in the upper mantle. Can. Mineral. 34, 1179–1193.

Griffin, W.L., Fisher, N.I., Friedman, J.H., O'Reilly, S.Y., Ryan, C.G., 2002. Cr-pyrope garnets in the lithospheric mantle: II. Compositional populations and their distribution in time and space. Geochem. Geophys. Geosyst. 3, 1073. https://doi.org/10.1029/2002GC000298.

Grütter, H.S., Gurney, J.J., Menzies, A.H., Winter, F., 2004. An updated classification scheme for mantle-derived garnet, for use by diamond explorers. Lithos 77, 841–857. https://doi.org/10.1016/j.lithos.2004.04.012.

Grütter, H., Latti, D., Menzies, A., 2006. Cr-saturation arrays in concentrate garnet compositions from kimberlite and their use in mantle barometry. J. Petrol. 47, 801–820. https://doi.org/10.1093/petrology/egi096.

Hanger, B.J., Yaxley, G.M., Berry, A.J., Kamenetsky, V.S., 2015. Relationships between oxygen fugacity and metasomatism in the Kaapvaal subcratonic mantle, represented by garnet peridotite xenoliths in the Wesselton kimberlite, South Africa. Lithos 212, 443–452. https://doi.org/10.1016/j.lithos.2014.09.030.

Hasterok, D., Chapman, D.S., 2011. Heat production and geotherms for the continental lithosphere. Earth Planet. Sci. Lett. 307, 59–70. https://doi.org/10.1016/j.epsl.2011.04.034.

Herzberg, C., Zhang, J., 1996. Melting experiments on anhydrous peridotite KLB-1: compositions of magmas in the upper mantle and transition zone. J. Geophys. Res. 101, 8271–8296. https://doi.org/10.1029/96JB00170.

Hirschmann, M., 1991. Thermodynamics of multi-component olivines and the solution properties of $(Ni,Mg,Fe)_2SiO_4$ and $(Ca,Mg,Fe)_2SiO_4$ olivines. Am. Mineral. 76, 1232–1248. https://doi.org/10.2138/am-2000-1030.

Holland, T.J.B., Powell, R., 2011. An improved and extended internally consistent thermodynamic dataset for phases of petrological interest, involving a new equation of state for solids. J. Metamorph. Geol. 29, 333–383. https://doi.org/10.1111/j.1525-1314.2010.00923.x.

Ionov, D., 2004. Chemical variations in peridotite xenoliths from Vitim, Siberia: inferences for REE and Hf behaviour in the garnet-facies upper mantle. J. Petrol. 45, 343–367. https://doi.org/10.1093/petrology/egg090.

Ionov, D.A., Doucet, L.S., Ashchepkov, I.V., 2010. Composition of the lithospheric mantle in the Siberian craton: new constraints from fresh peridotites in the Udachnaya-East kimberlite. J. Petrol. 51, 2177–2210. https://doi.org/10.1093/petrology/egq053.

Kopylova, M.G., O'Reilly, S.Y., Genshaft, Yu.S., 1995. Thermal state of the lithosphere beneath Central Mongolia: evidence from deep-seated xenoliths from the Shavaryn-Saram volcanic Centre in the Tariat depression, Hangai, Mongolia. Lithos 36, 243–255. https://doi.org/10.1016/0024-4937(95)00020-8.

MacGregor, I.D., 1974. The system $MgO-Al_2O_3-SiO_2$: solubility of Al_2O_3 in enstatite for spinel and garnet peridotite compositions. Am. Mineral. 59, 110–119.

Mofokeng, S.W., 1998. A Comparison of the Nickel and the Conventional Geothermometers with Respect to the Jagersfontein and the Matsoku Kimberlite Peridotite Xenoliths. Master Dissertation,. University of Cape Town, South Africa.

Nickel, K.G., Green, D.H., 1985. Empirical geothermobarometry for garnet peridotites and implications for the nature of the lithosphere, kimberlites and diamonds. Earth Planet. Sci. Lett. 73, 158–170. https://doi.org/10.1016/0012-821X(85)90043-3.

Nimis, P., 2022. Pressure and temperature data for diamonds. Rev. Mineral. Geochem. 88, 533–566. https://doi.org/10.2138/rmg.2022.88.10.

Nimis, P., Grütter, H., 2010. Internally consistent geothermometers for garnet peridotites and pyroxenites. Contrib. Mineral. Petrol. 159, 411–427. https://doi.org/10.1007/s00410-009-0455-9.

Nimis, P., Taylor, W.R., 2000. Single clinopyroxene thermobarometry for garnet peridotites; part I, Calibration and testing of a Cr-in-Cpx barometer an enstatite-in-Cpx thermometer. Contrib. Mineral. Petrol. 139, 541–554. https://doi.org/10.1007/s004100000156.

Nimis, P., Goncharov, A., Ionov, D.A., McCammon, C., 2015. Fe^{3+} partitioning systematics between orthopyroxene and garnet in mantle peridotite xenoliths and implications for thermobarometry of oxidized and reduced mantle rocks. Contrib. Mineral. Petrol. 169, 6. https://doi.org/10.1007/s00410-014-1101-8.

Nimis, P., Preston, R., Perritt, S.H., Chinn, I.L., 2020. Diamond's depth distribution systematics. Lithos 376–377, 105729. https://doi.org/10.1016/j.lithos.2020.105729.

O'Neill, H.St.C., Wood, B.J., 1979. An experimental study of Fe–Mg partitioning between garnet and olivine and its calibration as a geothermometer. Contrib. Mineral. Petrol. 70, 59–70. https://doi.org/10.1007/BF00371872.

Pardoe, I., 2021. Applied Regression Modeling. Wiley, 310 pp.

Rivalenti, G., Mazzucchelli, M., Laurora, A., Ciuffi, S.I.A., Zanetti, A., Vannucci, R., Cingolani, C.A., 2004. The backarc mantle lithosphere in Patagonia, South America. J. S. Am. Earth Sci. 17, 121–152. https://doi.org/10.1016/j.jsames.2004.05.009.

Ross II, C.R., Keppler, H., Canil, D., O'Neill, H.St.C, 1996. Structure and crystal-field spectra of $Co_2Al_2(SiO_4)_3$ and $(Mg,Ni)_3Al_2(SiO_4)_3$ garnet. Am. Mineral. 81, 61–66. https://doi.org/10.2138/am-1996-1-209.

Ryan, C.G., Griffin, W.L., Pearson, N.J., 1996. Garnet geotherms: Pressure–temperature data from Cr-pyrope garnet xenocrysts in volcanic rocks. J. Geophys. Res. 101, 5611–5625. https://doi.org/10.1029/95JB03207.

Smith, D., Barron, B.R., 1991. Pyroxene-garnet equilibration during cooling in the mantle. Am. Mineral. 76, 1950–1963.

Sobolev, N.V., Lavrent'ev, Y.G., Pokhilenko, N.P., Usova, L.V., 1973. Chrome-rich garnets from the kimberlites of Yakutia and their paragenesis. Contrib. Mineral. Petrol. 40, 39–52. https://doi.org/10.1007/BF00371762.

Sudholz, Z.J., Yaxley, G.M., Jaques, A.L., Chen, J., 2021. Ni-in-garnet geothermometry in mantle rocks: a high pressure experimental recalibration between 1100 and 1325 °C. Contrib. Mineral. Petrol. 176, 32. https://doi.org/10.1007/s00410-021-01791-8.

Taylor, W.R., 1998. An experimental test of some geothermometer and geobarometer formulations for upper mantle peridotites with application to the thermobarometry of fertile lherzolite and garnet websterite. Neues Jb. Mineral. Abh. 172, 381–408. https://doi.org/10.1127/njma/172/1998/381.

Viljoen, F., Dobbe, R., Smit, B., 2009. Geochemical processes in peridotite xenoliths from the Premier diamond mine, South Africa: evidence for the depletion and refertilisation of subcratonic lithosphere. Lithos 112 (Suppl. 2), 1133–1142. https://doi.org/10.1016/j.lithos.2009.05.004.

Viljoen, K.S., Harris, J.W., Ivanic, T., Richardson, S.H., Gray, K., 2014. Trace element chemistry of peridotitic garnets in diamonds from the Premier (Cullinan) and Finsch kimberlites, South Africa: contrasting styles of mantle metasomatism. Lithos 208, 1–15. https://doi.org/10.1016/j.lithos.2014.08.010.

Wu, C.M., Zhao, G.C., 2007. A recalibration of the garnet–olivine geothermometer and a new geobarometer for garnet peridotites and garnet–olivine–plagioclase-bearing granulites. J. Metamorph. Geol. 25, 497–505. https://doi.org/10.1111/j.1525-1314.2007.00706.x.

Yaxley, G.M., O'Neill, H.St.C., 2008. Ni in garnet thermometry – a new experimental calibration at 3.0–4.5 GPa of Ni-Mg exchange between garnet and olivine at upper mantle pressures. In: 9th International Kimberlite Conference Extended Abstract No. 9IKC-A-00200. https://ikcabstracts.com/index.php/ikc/article/view/3440/3440.

Yaxley, G.M., Berry, A.J., Kamenetsky, V.S., Woodland, A.B., Golovin, A.V., 2012. An oxygen fugacity profile through the Siberian Craton—Fe K-edge XANES determinations of $Fe^{3+}/\Sigma Fe$ in garnets in peridotite xenoliths from the Udachnaya East kimberlite. Lithos 140, 142–151. https://doi.org/10.1016/j.lithos.2012.01.016.

Zheng, J.P., Griffin, W.L., O'Reilly, S.Y., Yang, J., Li, T., Zhang, M., Zhang, R.Y., Liou, J. G., 2006. Mineral chemistry of peridotites from Paleozoic, Mesozoic and Cenozoic lithosphere: constraints on mantle evolution beneath eastern China. J. Petrol. 47, 2233–2256. https://doi.org/10.1093/petrology/egl042.

Ziberna, L., Nimis, P., Zanetti, A., Marzoli, A., Sobolev, N.V., 2013. Metasomatic processes in the central Siberian cratonic mantle: evidence from garnet xenocrysts from the Zagadochnaya kimberlite. J. Petrol. 54, 2379–2409. https://doi.org/10.1093/petrology/egt051.

Ziberna, L., Nimis, P., Kuzmin, D., Malkovets, V.G., 2016. Error sources in single-clinopyroxene thermobarometry and a mantle geotherm for the Novinka kimberlite, Yakutia. Am. Mineral. 101, 2222–2232. https://doi.org/10.2138/am-2016-5540.